Effect of deep cryogenic treatment on microstructure and properties of AE42 magnesium alloy

A thesis submitted in partial fulfillment of the requirements for the degree of

Master of Technology

in

Metallurgical and Materials Engineering

by

Pranav Bhale
(Roll No.: 213MM1463)

Department of Metallurgical and Materials Engineering
National Institute of Technology, Rourkela
May 2015

Effect of deep cryogenic treatment on microstructure and properties of AE42 magnesium alloy

A thesis submitted in partial fulfillment of the requirements for the degree of

Master of Technology

in

Metallurgical and Materials Engineering

by

Pranav Bhale

Under the guidance and supervision of

Prof. Ashok Kumar Mondal

Department of Metallurgical and Materials Engineering
National Institute of Technology, Rourkela
May 2015

Department of Metallurgical and Materials Engineering,

National Institute of Technology Rourkela,

Rourkela-769008

India

Certificate

This is to certify that the thesis entitled "**Effect of deep cryogenic treatment on microstructure and properties of AE42 magnesium alloy"** submitted by **Pranav Bhale** to National Institute of Technology, Rourkela is a record of bonafide research work under our supervision and is worthy of consideration for the award of the degree of Master of Technology degree in **Metallurgical and Materials Engineering** with specialization in **Metallurgical and Materials Engineering** of the Institute. The candidate has fulfilled all prescribed requirements for the thesis, which is based on candidate's own work and has not been submitted elsewhere for a degree or diploma.

Date: **Supervisor**

Place:

Prof. Ashok Kumar Mondal

Dept. of Metallurgical and Materials Engg.

National Institute of Technology

Rourkela-769008

TABLE OF CONTENTS

Acknowledgements

I am using this opportunity to express my thanks to Department of Metallurgical and Materials Engineering, National Institute of Technology, Rourkela for offering an exclusive platform to earn exposure and gather knowledge.

I wish to extend my sincere and deepest gratitude to my guide Prof. A. K. Mondal, a true guide who supported and encouraged me during the entire tenure of the project. He inspired me to drive this thesis towards the path of glory and success.

I also thank to Prof. S. C. Mishra, the HOD, Department of Metallurgical and Materials Engineering, National Institute of Technology Rourkela for granting me permission to do this project and avail all the facilities in the department. I also express my thanks to all other Professors of our department for their co-operation and valuable advice during the course work and my project work.

I am grateful and thankful to the technical assistants Mr. K.Tanty, Mr. A. K. Acharya, and Mr. S. Pradhan for the support they rendered during the execution of my project. I feel a great pleasure to acknowledge some of my lab mates like Mr. Anil Kumar Singh Bankoti and Mr. Hrishikesh Shastri who helped me by providing multiple ideas throughout the completion of my thesis. I would also like to thank my colleagues Rajneesh Pandey, Lala Amarnath and Meet Shukla for their support and assistance in multiple phases of the work.

My acknowledgment will be incomplete without expressing my gratitude towards my family and to Almighty, for their blessings and for being constant source of encouragement.

Place: Rourkela Pranav Bhale

Abstract

There has been a great interest of using magnesium (Mg) alloys in automotive industries owing to its high specific strength, high thermal conductivity, good damping capacity and good machinability. The use of Mg alloys in automobile increases fuel efficiency and reduce emissions by reducing the vehicle weight. The AE42 alloy is a promising creep resistant Mg alloy and it is suitable for application up to 175°C.

Cold treating is a very old process and is widely used for high precision parts to enhance their properties. Cold treatment can be done in 2 ways. When treatment is done at temperature down to -80°C it is called 'Cryogenic Treatment (CT)'. On the other hand, when treatment is done at liquid nitrogen temperature (i.e., -196°C) it is called 'Deep Cryogenic Treatment (DCT)'. Deep cryogenic treatment generally improves certain properties beyond the improvement obtained by normal cryogenic treatment. When CT was carried for steel, it was observed that there was complete transformation of retained austenite into martensite. Also, there was improvement of mechanical properties which can be explained by the precipitation of submicroscopic carbides as a result of the CT. When deep cryogenic treatment was carried out on steel, it showed significant increase in wear resistance. It was theorized that the increase in wear resistance was a direct result of the reduction in the amount of retained austenite and change in the carbide morphologies. Therefore, it is concluded that DCT has pronounced effect to alter microstructure and thereby the mechanical properties. The number of literature that report DCT of different kinds of steels, ZnO nanowires and pure Zr is plenty. Unfortunately, the number of literature on CT/DCT for Mg alloy is rare. Recently, CT/DCT on AZ91 and AZ31 Mg alloys resulted homogeneity in microstructure that exhibited superior wear and tensile properties. However, the

precise effect of CT/DCT on properties like hardness, creep, corrosion and so on is still not clear. Therefore, in the present study, mechanical properties including wear as well as corrosion behavior of the AE42 (Mg-4Al-2RE) Mg alloy subjected to DCT is planned for investigation. For comparison the same tests will be carried out on AE42 alloy without DCT. DCT was carried out on specimens for 0, 4, 8 and 16 h. A detailed microstructural characterization of the untreated and treated AE42 alloy has been done. The specimens were prepared according to required dimensions for the above-mentioned tests. The phase analysis using XRD as well as optical and SEM micrographs were taken on the untreated and treated AE42 alloy. It was observed that with increase in DCT time the volume fraction of secondary Al_4RE phase was reducing and that of primary α-Mg was increasing. Tensile, hardness, wear and corrosion tests were carried out on all specimen and its results were compared. The ductility of tensile specimens was increasing with increase in DCT time. The hardness of the specimens decreased with increase in DCT time. The wear rate increased with increase in DCT time. Corrosion specimens showed increase in corrosion rate with increase in DCT time.

LIST OF FIGURES

LIST OF TABLES

Chapter 1

INTRODUCTION

1.1 Introduction

Over the past few years, scarcity of energy resources, escalating fuel prices and stricter emission norms has led industries to search for novel and advanced materials as a substitute for conventional materials. Choice of lightweight metals is an obvious solution to this problem. Magnesium (Mg), being the sixth most abundant element in earth's crust [1], is one such promising metal which is useful to many engineering applications in automobile, aerospace industries etc. Due to lower density compared to other structural metals like Aluminum (Al), Iron (Fe) etc., Mg has substantial impact on environment (by reducing emission of greenhouse gases). Other key features include superior specific strength, high thermal conductivity, good castability etc. These properties can further be enhanced by addition of different metals, like Al, Zinc (Zn), Manganese (Mn) and many others, to Mg to form an alloy. A good balance between strength and ductility has led to extensive use of Al containing Mg alloy (like AZ91). But these alloys lack in high temperature properties (near to 120°C), specifically creep properties, which limit their applications. Presence of discontinuous secondary β-phase ($Mg_{17}Al_{12}$) leads to reduced creep properties [2, 3, 4]. There are many ways to improve the properties of an alloy. One of them is by changing the volume fraction of intermetallic compound in microstructure of these alloys can help in improving these properties. Addition of different alloying elements helps in achieving this. For example, by adding Ca to AZ91 Mg alloy, creep resistance at elevated temperature can be improved. Ca helps in breaking down the dendritic morphology found in these alloys and refines grain [3, 4]. Considering this, many alloy systems have been developed to improve high temperature properties by suppressing β-phase. AE42 alloy (i.e., Mg-Al-RE system) was developed for the purpose. Powell et al. [5] investigated the change in microstructure in AE42 alloy, on which creep tests were carried out at 150°C and 175°C. They observed that there was

absence of β-phase and presence of $Al_{11}RE_3$ intermetallic phase at 150°C whereas at 175°C this $Al_{11}RE_3$ decomposed to Al_2RE phase. The remaining Al again reacted with Mg to form β-phase.

Another way of improving the properties of an alloy is to carry out temperature controlled treatment. Heat treatment is a common practice followed from earlier ages whereas Cold treatment is a much newer method followed to study the changes in properties of the alloy. Cold treatment is a process used to check the ability of the material to perform at low temperatures. It can be done in 2 ways: "cold treatment (CT)"which is done at temperatures near to −80 °C and "deep cryogenic treatment (DCT)", which is done using liquid nitrogen (nearly −196°C). DCT improves certain properties beyond the improvement obtained by ordinary cold treatment [6]. In general a basic CT/DCT process consists of cooling the specimen gradually up to a particular temperature and then holding it for a given period of time and then bringing it back to room temperature [7]. DCT can be carried out on components to improve its mechanical properties, which can help in improving performance and life of components. Also, DCT shows control in distortion of metal objects and improves vibrational characteristics of metals. Not much work has been done to study the effect of DCT on Mg alloy, which has been the driving force behind carrying out this investigation.

1.2 Objective

In the present investigation DCT was carried out on the AE42 alloy for 4, 8 and 16 h. The effect of DCT on microstructure and properties of the AE42 alloy was evaluated.

Chapter 2

LITERATURE REVIEW

This chapter consists of the literature that have been significant for the completion of this thesis. This section consists of seven parts. Part 1 consists of a brief introduction to elemental Mg and its properties. Part 2 consists of uses of Mg and its alloys. Part 3 a brief explanation on Mg alloy naming conventions. Part 4 consists of description on Mg-Al-RE alloys and AE42 alloy. Part 5 consists of synthesis techniques Mg-based alloys. Part 6 consists of literature related to DCT and its effects on different materials. Part 7 consists of an explanation related to mechanisms involved in tensile, hardness, corrosion and wear tests.

2.1 Magnesium and its properties

The origin of the word Magnesium (Mg) comes from Greek word Magnesia which is a district in Thessaly, Greece. In 1808, British chemist Sir Humphrey Davy carried out electrolysis on a mixture of magnesia (magnesium oxide, MgO) and mercuric oxide (HgO) and obtained elemental Mg. It was extensively used in World War II, mainly for aircrafts. Mg is an alkaline earth metal which is also the sixth most abundant metal found in earth crust. Some of the atomic properties have been mentioned in Table 2.1. It has a crystal structure of hexagonal close packed (hcp). At room temperature it can be observed that pure Mg has the following lattice parameters: a= 0.32092 nm and c= 0.521025 nm, with a c/a ratio of 1.633. Adding solute elements to Mg crystal structure increases the lattice parameter of the Mg unit cell. Wu et al. [9] reported the increase in c/a ratio of Mg by adding rare earth elements like Gd, Dy and Y.

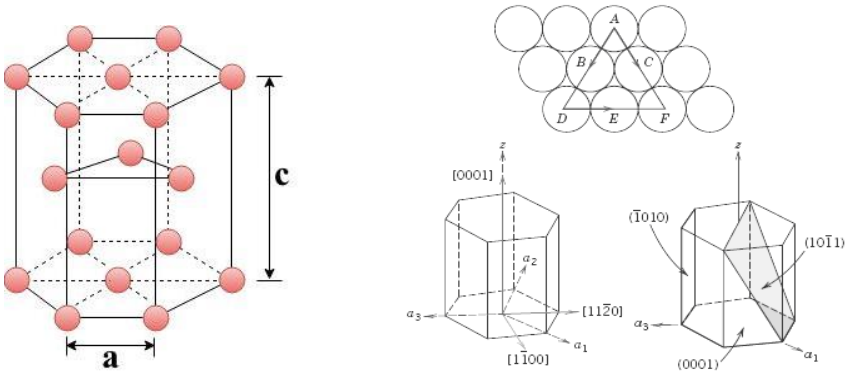

(a) (b)

Fig. 2.1: (a) Hexagonal closed packed (HCP) crystal structure of Mg (b) Slip planes in HCP

Table 2.1: Properties of pure Mg

Density (at 20°C)	1.738 g/cm^3
Melting point	650°C
Thermal conductivity	156 W/m K
Specific heat capacity	1.025 kJ/kg K
Elastic modulus	45 GPa
0.2% Proof stress	75-200 MPa
Ultimate tensile strength	135-285 MPa
Elongation	2-10%

2.2 Applications of Mg alloys

2.2.1 Automotive

The use of Mg for a particular component can be determined based on the requirement. Fig. 2.2 shows the different requirements of vehicle component for an automotive application. Mg shows properties that make it a requirement for rigidity and strength. In general, a vehicle consists of transmission system, interior, body and chassis, where Mg finds potential applications. Fig. 2.3 shows the demand properties of different vehicle components.

It was in 1930s when Mg found its first application in commercial vehicles. The Volkswagen (VW) Beetle was equipped with Mg alloy in its transmission system. Till date many manufacturing companies use Mg alloy to develop transmission systems. A transmission system consists of engine with manifolds, gearbox and drive shafts. As high temperature reaches inside the engine (i.e. crankcase), it is here where Mg alloys find their application. The VW Beetle had a crankcase made of AS41 alloy which had a weight near to 10 kg. It helped in saving the weight of the engine by 25% compared to the vehicles using Al crankcase. The reason why Mg alloys are used in engines is due good creep resistance at 150-200°C. A sports car engine-crankcase has a requirement of less vibrational properties, where the use of Mg alloys like WE54, QE22 etc. come into account [11]. For cost effective alternatives, Mg alloys like MRI201S, MRI230D etc. are used [12]. In the interior of a vehicle Mg alloys can be used in steering wheels, seats, levers and housings. Light weight, good energy absorption and high strength are some requirements in interiors of vehicle which are fullfiled by Mg alloys. The core of steering wheel in VW Golf is uses AM50 alloy. Reduction in weight, stiffness and surface quality are few features required for body of a vehicle.

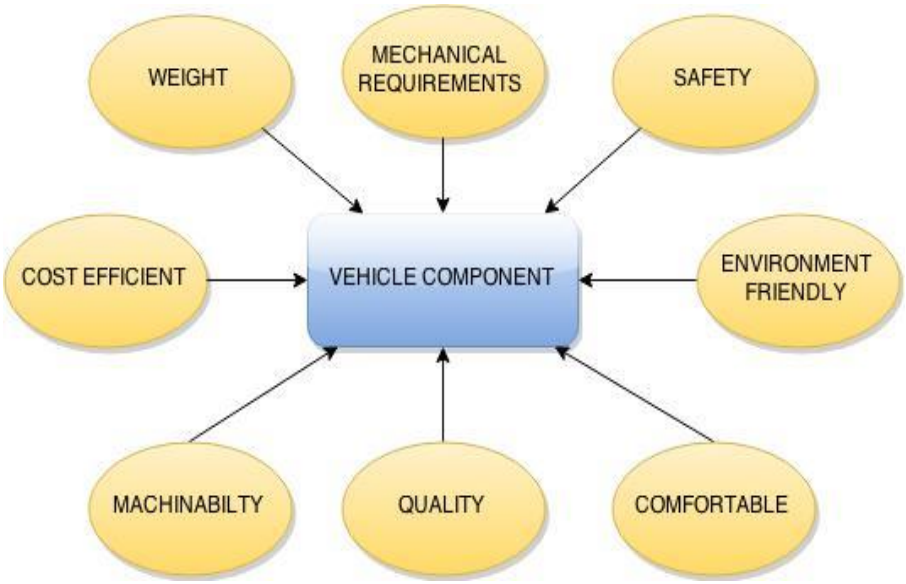

Fig. 2.2: Requirement of vehicle component

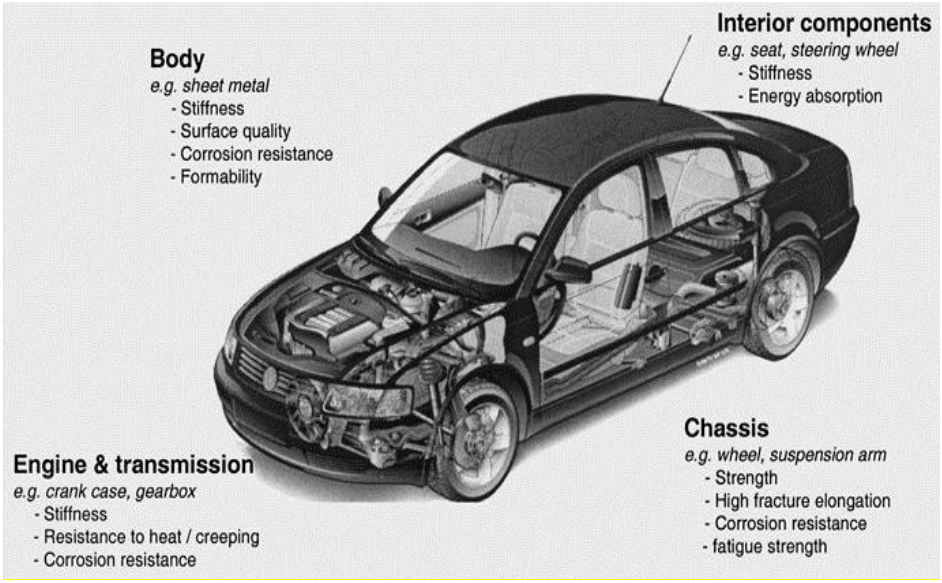

Fig. 2.3: Potential use of Mg in vehicle component [10]

In general, Al is used in manufacturing the body frame of a vehicle. It was in tailgate of VW 3L Lupo, where Mg was used with Al in different proportions, for the very first time. The chassis of a vehicle (which consists of suspensions and wheels) must have good strength, light weight, corrosion resistant and should not have porosity. In 1970s, Porsche developed wheel using AM60, which was 19% lighter than forged Al wheel [13].

2.2.2 Aerospace

In recent years, increase the need of reduced weight in aircrafts has lead researchers to use materials that not only gave low density but should also be cost efficient. Al alloys, fiber metal laminates (FML) and structural plastics have been used vastly for this purpose. Limited innovation in development of Al alloys, expensive FML and low impact properties of structural plastics have lead Mg to be used as an alternative in this application. Mg has been frequently used in manufacturing of military as well as ordinary aircrafts and helicopters. The Focke Wulf Condor 200, a civilian aircraft, consisted of engine, fuselage and wing components made of AM503 alloy, which is considered to be one of the most weldable metal alloy [14]. In World War II Mg sheets were used to fabricate aircraft parts. The B-36 Bomber, US XP56 and F-80 fighter planes were made of rolled Mg [15].

2.2.3 Medical

Mg has low density and properties like compressive yield strength, elastic modulus and fracture toughness comparable with natural bone. So, it is considered to be a good biomaterial compared to other implant materials [16]. Mg is present in human body in small traces and is required for

essential metabolic processes. It is non-toxic and is bio-degradable. Mg has lower corrosion resistance under the influence of bio fluids, but in recent past addition of different alloying elements and surface protection coatings have been developed [18, 19, 20].

2.2.4 Sports

Excellent specific strength and good castability to manufacture attractive and intrinsic structures have led Mg to be used in different sports equipment. Some of the applications include golf clubs, handles of archery bows and head of tennis rackets. Due to good damping properties and light weight Mg based alloys find use in bicycle frames which should be adept to absorb shocks and vibration [10].

2.2.5 Electronic

Electronic industries aim for making products which are not only stylish but also portable and lightweight. Mg based materials, which not only are light and show high strength but also have ability to block electromagnetic radiations and other high frequency interferences, find their application in electronic products [10]. Cellphone and music player cases, laptop and computer housings are some fields where Mg alloys are used.

2.3 Mg alloy designation

American Society for Testing and Materials (ASTM B275) has given the abbreviation for alloying elements and designation procedure for Mg alloys. Table 2.2 shows abbreviation for some of the commonly used alloying elements. The designation consists of three parts. Part 1 consists of the initial alphabet of 2 main alloying additions in abbreviated form as per ASTM

standards. Part 2 consists of weight percentage of the 2 main alloying additions in the same order. Part 3 distinguishes between the different alloys with same weight percentage of alloying additions. It is an alphabet according to ASTM standards shown in Table 2.3.

Table 2.2: ASTM designation of alloying elements commonly used for Mg alloy

Abbreviation letter	**A**	**E**	**K**	**M**	**Q**	**S**	**W**	**Z**
Alloying element	Al	Rare earth metals	Zr	Mn	Ag	Si	Y	Zn

Table 2.3: Alloying designation as per ASTM standard

A	First compositions
B	Second compositions
C	Third compositions
D	High purity
E	High corrosion resistance
X	Experimental alloy

2.4 Mg-Al-RE system

The Rare earth elements include elements like Cerium (Ce), Lanthanum (La), Neodymium (Nd), Praseodymium (Pr), Thorium (Th). Being expensive these elements are added as master alloy called misch metal which is relatively cheaper. These elements have the property to improve creep resistance of Mg alloy [21, 22]. This alloy system consists of AE41, AE42, AE22 alloys.

The improved creep properties exhibited by the Mg-Al-RE alloy system is attributed to the suppression of the formation of β-phase (i.e. $Mg_{17}Al_{12}$) and due to the presence of Al-RE

intermetallic (in general $Al_{11}RE_3$ and Al_2RE) [3, 22, 23]. Powell et al. [5] investigated the microstructure of AE42 alloy at room temperature, 150°C and 175°C. They reported reducing wt.% of β-phase and increasing wt.% of $Al_{11}RE_3$ and Al_2RE phases as shown in Table 2.4. In general, RE have poor melt recovery after casting, which can be improved by use of protective gas surrounding.

Table 2.4: Wt.% of intermetallic compounds in AE42 alloy in different creep test conditions

Phases	Testing conditions		
	Room temperature	150°C	175°C
Mg	97.5	97.7	97.0
$Mg_{17}Al_{11}$	0.0	0.0	0.6
$Al_{11}RE_3$	1.8	1.5	1.2
Al_2RE	0.0	0.8	1.3

Lu et al. [22] studied the effect of addition of RE (in different wt.%) on the microstructure, properties and fracture behavior of AZ91 alloy. RE addition improved the fluidity and hardness of the alloy. It also improved the high temperature tensile properties of the alloy. All these changes were attributed to the formation of rod like $Al_{11}RE_3$ phase which reduced the $Mg_{17}Al_{12}$ phase present in the alloy.

Zhang et al. [23] investigated the phase composition, tensile properties and corrosion behavior of Mg-4Al-4RE-0.4Mn alloy. The microstructure consisted of 3 phases: α-Mg, $Al_{11}RE_3$ and Al_3RE phases. UTS and YS showed higher values at room temperature compared to that at 200°C. Better tensile properties were due to the presence of fine secondary phases present along the

grain boundaries. Addition of RE improved the corrosion resistance of the alloy due to presence of corrosion product film of Al and Ce/La.

2.5 Synthesis of Mg alloys

Over the years many techniques have been endeavored for the synthesis of Mg based alloys. The microstructural features obtained are highly dependent of the synthesis process followed. In general there are two categories of synthesis namely liquid phase and solid phase synthesis methods [24]. Due to lower processing cost and good ductility, liquid phase method is preferred over solid phase method. Liquid phase synthesis includes casting processes like sand casting, die casting, squeeze casting, stir casting, spray forming and in-situ synthesis. Mg alloys having RE are generally casted using sand casting and squeeze casting techniques [25] whereas Mg-Al alloys are synthesized using investment casting technique. From the many casting techniques used to obtain Mg alloys, squeeze casting is the area of concentration in this thesis work.

2.5.1 Squeeze-casting

The process of squeeze-casting combines the effects of forging and casting processes. The 2 types of squeeze-casting includes direct and indirect squeeze-casting methods. In the direct squeeze-casting, as shown in Fig. 2.4 (a), molten metal is poured into the lower die and pressure is applied by the upper die, to obtain the required shape of the cast. In the indirect squeeze-casting, as shown in Fig. 2.4(b), the lower die is filled using a runner system. The speed of molten metal can be adjusted with the help of a plunger. The melt in contact with the plunger solidifies first. The speed of the plunger determines the solidification time, turbulence and number of gas inclusions in the cast.

Some of the advantages of direct squeeze-casting over indirect squeeze-casting include absence of runner system leading to higher material yield, optimum cost and pore free cast is obtained due to uniform solidification pressure applied on the cast. Mg metal matrix composites (MMCs) are generally manufactured using direct squeeze-casting technique. Due to low cost of separation and manufacturing of intrinsic shaped cast, indirect squeeze-casting is generally used for infiltrating preforms of MMCs.

On the whole, squeeze-casting is used for synthesizing alloys which have a small solidification rate, due to which it is useful for Mg alloys. A typical microstructure of squeeze-casted AZ31 alloy, as shown in Fig. 2.5 [26], shows the α-Mg and β-$Mg_{17}Al_{12}$ intermetallic phases on the grain boundaries. Due to slower cooling, larger grain size was observed.

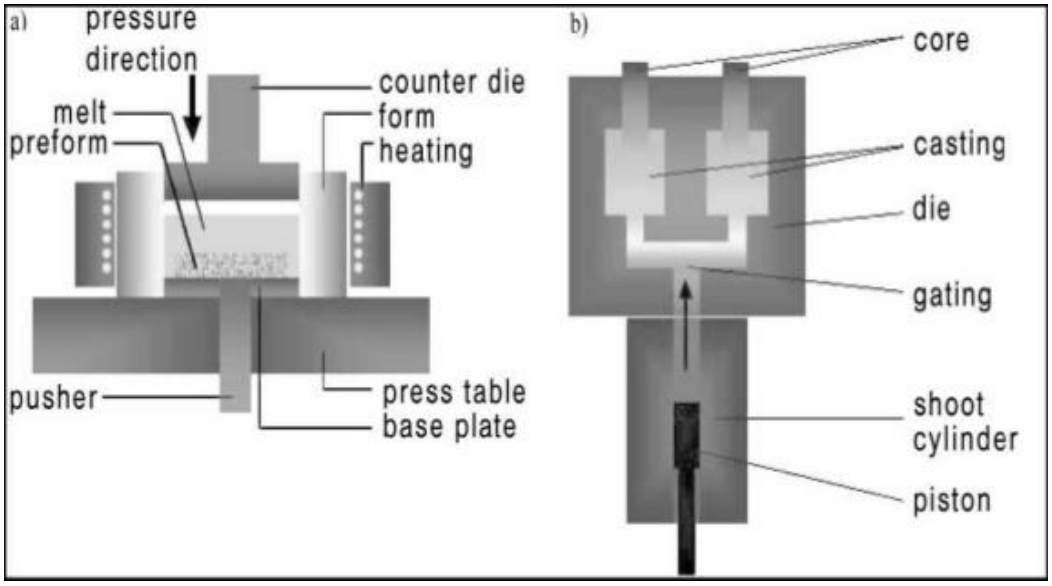

Fig. 2.4: Schematic diagram of (a) direct and (b) indirect squeeze-casting

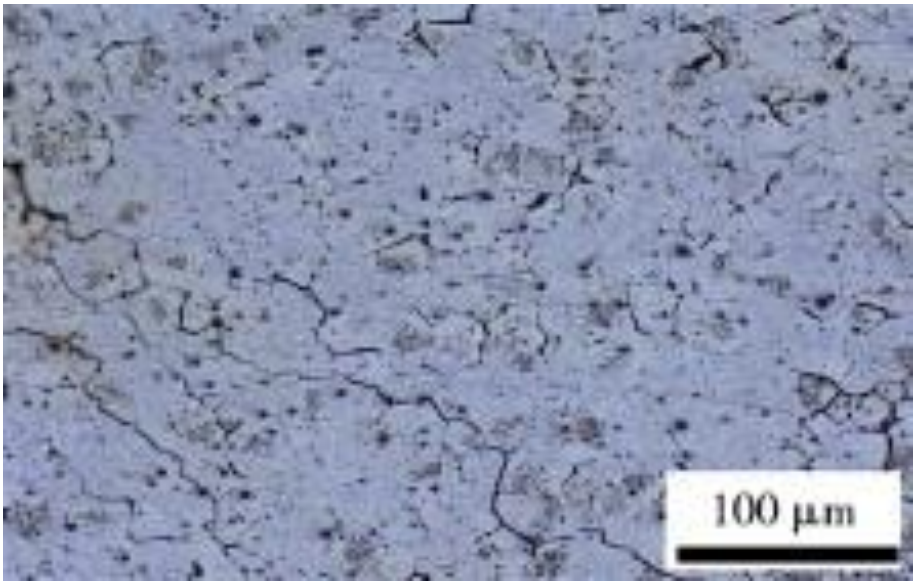

Fig. 2.5: Microstructure of squeeze-cast AZ31 alloy

The processing variables that govern the microstructural evolution of squeeze-cast alloys are:

a) Initial temperature of alloying addition

b) Squeeze pressure and speed of plunger

c) Speed of molten metal during pouring

2.6 Deep Cryogenic Treatment (DCT)

Since many years, thermal treatments are generally carried out on materials to enhance their properties according to the requirement. It is usually done by either heating or by cooling the material with respect to room temperature. Cold treatment had found its application since early 20^{th} century compared to Heat treatment which was in use since a very long time. Cold treatment is carried out at temperatures near to -80°C. The treatment carried out near to -150°C is called cryogenic treatment whereas when liquid nitrogen is used as cryogen (liquid nitrogen temperature i.e. -196°C) the process is called deep cryogenic treatment (DCT). The basic process involved in all types of cold treatment is to cool the material up to a definite temperature, holding it at that temperature for selected time period and then gradually bringing it back to the room temperature. Fig. 2.6 shows a temperature-time plot showing carious phases of cooling [7].

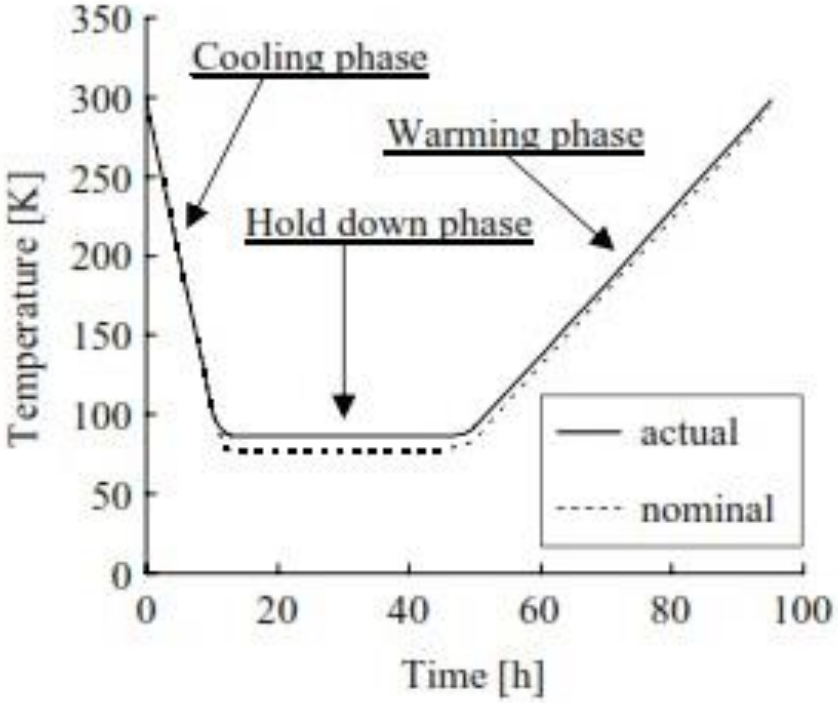

Fig. 2.6: Temperature-Time curve for cold treatment

Initially interest was found in DCT on different types of steels and other ferrous alloys. It was observed that DCT resulted in following changes:

a) Complete transformation of austenite to martensite
b) Fine carbide precipitates dispersed into the matrix
c) Elimination of residual stresses

Zhirafar et al. [27] carried out DCT on AISI 4340 steel. They calculated the volume% of retained austenite before and after DCT using neutron diffraction method. It was observed that the volume% of retained austenite reduced from 5.7% to 4.2%. Leskovek et al. [28] investigated the influence of DCT on microstructure of vacuum heat treated high speed steel. The microstructure of the alloy post DCT showed rod-like carbide precipitates apart from reduction in retained austenite. The same type of precipitates were obtained the alloy post tempering but the one obtained after DCT revealed more dimensional stability. They also reported an increase of Rockwell C hardness value by 5.26 % post DCT. The performance of cryo-treated HSS tool steel was carried out by da Silva et al. [29]. They found out that the XRD peaks of 25% of retained austenite before DCT transformed to martensite and fine carbide precipitates. They also found out that DCT improved the tool life by 44 % whereas no significant changes were observed in case of hardness of the tool. Huang et al. [30] carried out DCT on M2 tool steel. It was observed that the presence of spherical Fe_4M_2C (where M is W, Mo, Cr or V) carbides after DCT increased from 5 to 11%. They suggested that due to DCT internal stresses were generated which lead to generation of dislocations. These dislocations were the main cause for the segregation of carbon and alloying addition atoms. This localized diffusion depended on the holding time of material under DCT.

DCT was also carried out on some non-ferrous materials. Indumathi et al. [31] investigated the effect of DCT on wear of different types of polymers and composites. Marginal increase in crystallinity of polyetherimide (PEI) and polyimide (PI) was observed after DCT meanwhile, polytetraflouroethylene (PTFE) showed no changes in crystallinity. They related the increase in wear resistance of PEI and PI to the change in crystallinity which was then confirmed with SEM images of worn surfaces. They attributed these changes to the generation of residual stresses in the polymers. PTFE also showed improvement in wear resistance which was related to the hardness improvement. Lulay et al. [32] performed DCT on 7075 aluminum alloy. No changes were observed in tensile, impact and hardness properties of the alloy. When DCT was carried out on AZ91 Mg alloy by Asl et al. [6] to investigate its effect on microstructure, wear and creep properties of the alloy, it was observed that the morphology of the β-$Mg_{17}Al_{12}$ intermetallic phase changed. The coarse divorced eutectic β phase penetrated into the matrix which strengthened the matrix phase. This change was attributed to the improvement of wear resistance of the treated alloy. Lower creep rates were observed for the treated alloy where dislocation creep was observed as the major creep mechanism.

2.7 Mechanical properties

2.7.1 Tensile

Tension can be defined as the pulling force acting on the body across its ends. It can either be uniaxial, biaxial or triaxial. This thesis work deals with the uniaxial tension, which is widely used to obtain design data on the strength of materials. In uniaxial tension test the specimen is subjected to an increasing uniaxial load. The changes in the elongation of the specimen are

noted. The data obtained is plotted as engineering stress-strain curve. The engineering stress (s) as described in equation 1 is the ratio of load (P) to the original area of cross-section of the specimen (A_0). A typical engineering stress-strain curve is shown in Fig. 7 [33].

$$s = \frac{P}{A_0} \tag{1}$$

The engineering strain (e) is obtained by dividing change in length (ΔL) by the original length of the specimen (L_0) as shown in equation 2

$$e = \frac{\Delta L}{L_0} = \frac{L - L_0}{L_0} \tag{2}$$

From the Fig. 2.7 it can be observed that initially the specimen undergoes elastic deformation where there is linear proportionality between stress and strain. When the stress exceeds a value (yield strength), the specimen undergoes plastic deformation. Beyond yield strength if the load is removed the specimen will remain permanently deformed. To continue the plastic deformation the strain is increased. This is where the specimen strain hardens. The volume of the specimen remains constant throughout the process. Initially, the strain hardening is more than the decrease in cross sectional area. At a particular point, the decrease in cross sectional area exceeds the load required to continue strain hardening. This point is the ultimate tensile strength (UTS or S_u) of the specimen beyond which necking starts and the engineering stress starts to decrease. The necking continues up to the point of failure or fracture of the specimen.

$$s_u = \frac{P_{max}}{A_0} \tag{3}$$

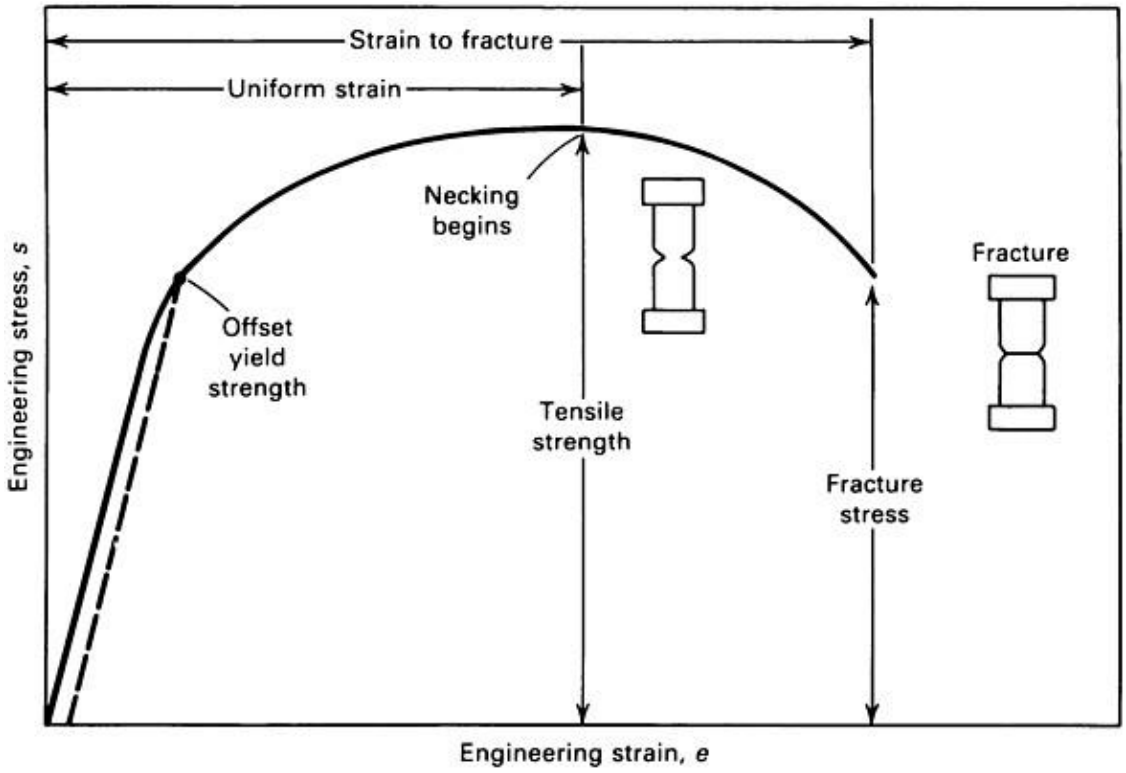

Fig. 2.7: Engineering stress-strain curve

For most materials a gradual change is observed from elastic to plastic behavior. Usually it is difficult to distinguish between elastic limit, proportional limit and yield strength. The yield strength of specimen is calculated as 0.2 % offset yield strength (s_0) as shown in equation 4. It is the stress corresponding to 0.2% strain.

$$s_0 = \frac{P_{(strain\ offset=0.002)}}{A_0} \tag{4}$$

2.7.2 Hardness

The property by virtue of which a material resists plastic deformation is called hardness. The different types of hardness tests include Brinell hardness test, Vickers hardness test, Rockwell hardness test etc. This thesis work includes Vickers hardness test, whose mechanism is mentioned below.

The indenter used in Vickers hardness test is a diamond type with square based pyramid base which has sides inclined to each other at 136°. Initially a load (P) is applied to the surface for a particular dwell time after which it is removed. The indent formed due to applied load is seen under microscope. The 2 diagonals (d_1, d_2) of the square indent are measured. The hardness value (HV) is calculated using equation 5. Fig. 2.8 shows the schematic diagram of the hardness test.

$$HV = \frac{2P\ Sin(\frac{136}{2})}{d^2} = \frac{1.854P}{d^2} \tag{5}$$

By visually examining, the hardness of the material depends on the size of indent formed. A material will be harder having small size of indent.

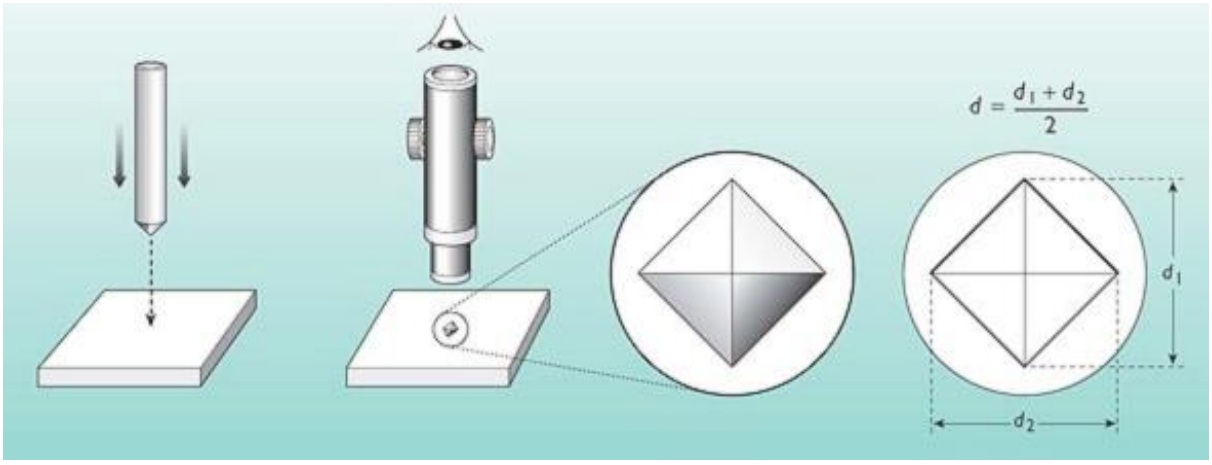

Fig. 2.8: Steps involved in performing Vickers hardness test

2.7.3 Wear

Wear can be defined as the loss of material from the surface of material due to relative motion with another material. The different types of wear include: abrasive wear, polishing wear, erosion wear, sliding and adhesive wear, fretting wear and corrosion wear. This present study focuses on abrasive wear. Abrasion wear occurs when hard particles are forced to move along a solid surface. Asperities are provided on the specimen surface so that both surface can move relative to each other owing to friction. On the basis of type of contact abrasion can be classified as two-body and three-body wear. When abrasive slides along surface, it is called two-body wear, whereas, when abrasive comes in between the two surfaces it is called three-body wear. The different mechanisms involved in abrasion wear include: ploughing, wedge formation, cutting, fragmentation and microcracking. The process in which the material is removed from the grooves to the outer sides of the grooves is termed as Ploughing. In cutting the material is separated in form of chips form the surface. When shear strength of the removed material exceeds the shear strength of the contact interface, wedge is formed ahead of the abrasive tip. Fragmentation occurs when cracks are formed around the wear groove and these cracks generate smaller cracks called microcracks which are formed along with removal of material. Ploughing, wedge formation and cutting are the phenomena observed with ductile materials whereas fragmentation and microcracking occurs with brittle materials.

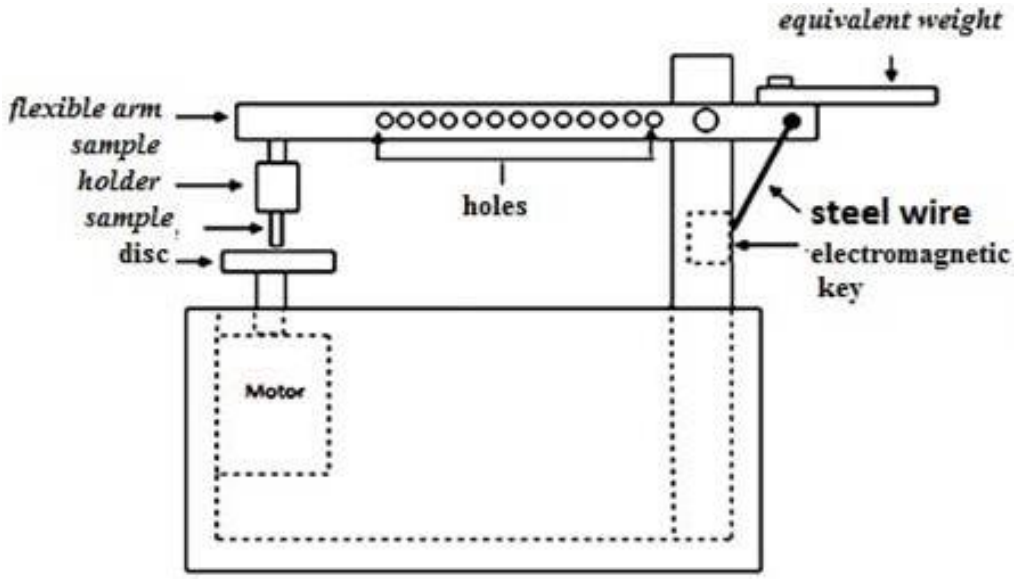

Fig. 2.9: Schematic of ball on disc type wear testing apparatus

There are many methods to carry out a wear test. The most common method is the ball on disc type of apparatus as shown in Fig. 2.9. A ball of a particular material is loaded against flat sliding surface (test specimen), which is rotated with the help of a motor. Counterweight and wear diameter are set according to experiment. The weight loss from the disc is measured. Wear depth (in μm) and sliding distance (in mm) are recorded and it is plotted as a function of wear depth

.

2.7.4 Corrosion

Corrosion can be defined as the deterioration of a metal due to environmental condition. It occurs as two or more electrochemical reaction on the surface of the metal due to its reaction with the surrounding. The products of corrosion may dissolve or remain in solid form. A corrosion test is performed to predict the corrosion behavior, for material selection, for environmental behavior and to study the corrosion mechanism. The electrochemical tests are performed in 2 ways. Short period corrosion test called as potentiodynamic polarization test and long period corrosion test called AC electrochemical impedance spectrum (EIS) test. The potentiodynamic polarization test is the area of concern in this thesis work. This test is carried out with the help of a power supply called potetiostat. It consists of 3 electrodes: an auxiliary electrode which supplies current to a working electrode (i.e. test specimen) and a reference electrode. Fig. 2.10 shows the experimental setup of the electrochemical polarization test. The potential developed between working and reference electrode due to their reaction in electrolyte is examined in this test. When the working electrode, immersed in electrolyte, is not connected to any power supply, the potential observed is corrosion potential (E_{corr}). At E_{corr} rate of oxidation is equal to the rate of reduction. When the specimen gets polarized the anode current dominates the cathode current.

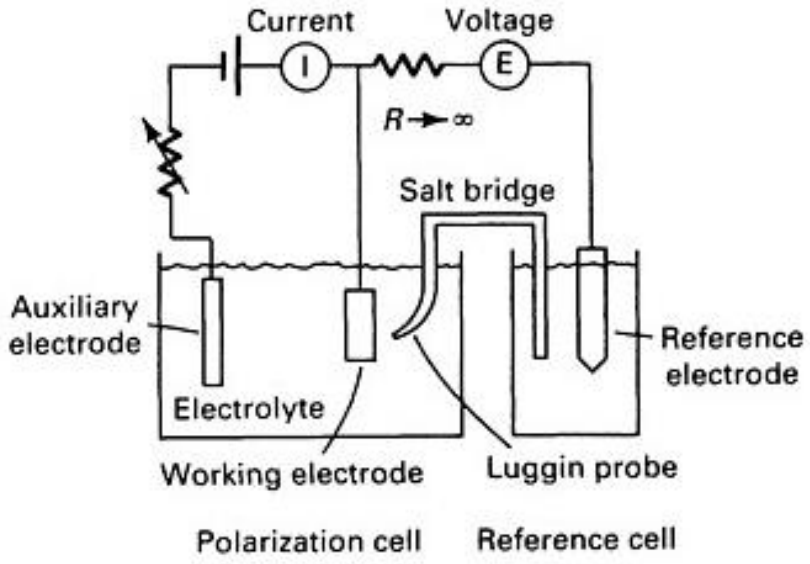

Fig. 2.10: Schematic of electrochemical corrosion testing setup

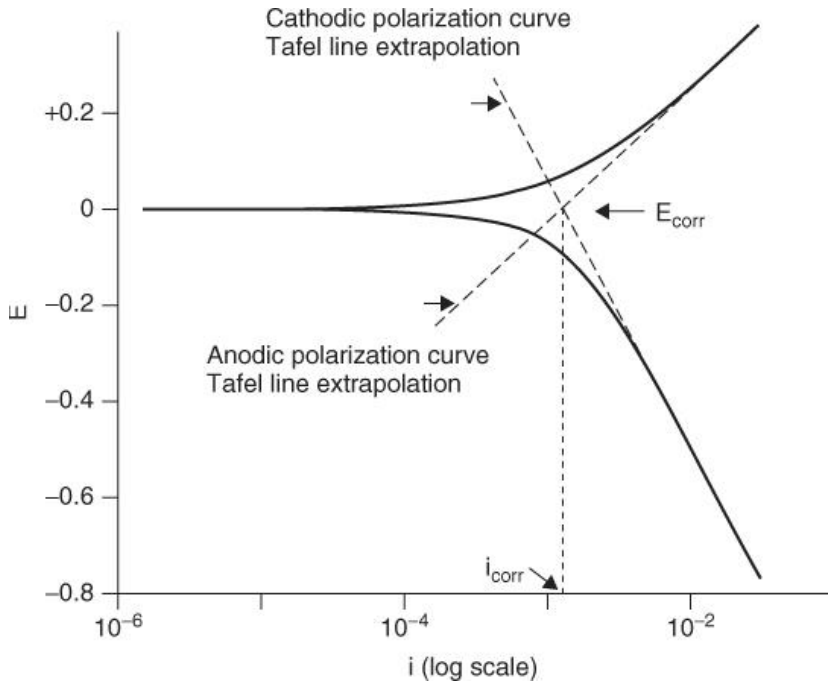

Fig. 2.11: Tafel curve showing E_{corr} and i_{corr} values

This change in the electrode potential owing to a net current is called polarization. The polarization characteristics are plotted as current (log current) as function of applied potential. Fig. 2.11 shows the semi-log plot of the polarization test [34]. These plots are also called Tafel curves. The E_{corr} and i_{corr} values are found out by extrapolation method. Potentials that are negative to the E_{corr} develop the cathodic currents whereas those positive to the E_{corr} develop the anodic currents. The i_{corr} (in μA) values can also be found out by the equation 6, where β_A and β_C are Tafel constants measured from the Tafel curve and $\Delta E/\Delta i$ is the slope of polarization curve.

$$i_{corr} = \frac{\beta_A \beta_C}{2.3\ (\beta_A + \beta_C)} \frac{\Delta E}{\Delta i} \quad (6)$$

The corrosion rate (in mils per year or mpy) can be calculated using equation 7.

$$Corrosion\ Rate = \frac{534W}{\rho AT} \quad (7)$$

Where,

W = weight loss of the specimen (in mg)

ρ = density of specimen (in gm/cm^3)

A = area of specimen (in^2)

T = exposure time (in hours)

Chapter 3

MATERIALS AND EXPERIMENTAL PROCEDURE

3.1 Material fabrication

The chemical composition of the AE42 alloy is given in Table 3.1. Here, rare earth elements are added as misch metal in the form of master alloy. Fabrication of the alloy was done using direct squeeze-casting technique. The materials as mentioned in Table 3.1 were melted in furnace up to 770°C. The melt was then passed through a pathway and poured into a die (both preheated to 250°C). A vertical pressure of 100 MPa was applied by upper ram of vertical hydraulic press for nearly 20 seconds. The speed of ram was maintained at 10mm/s. After complete solidification, the cast was obtained by removing the lower die.

Table 3.1: Composition of the AE42 Mg alloy

Materials	**Wt.%**
Magnesium	Bal.
Aluminum	4%
Rare earth	2%
• Lanthanum	0.6%
• Cerium	1.2%
• Neodymium	0.4%
• Thorium	0.6%
• Praseodymium	0.1%

3.2 DCT of the specimens

After preparing specimens for different tests according to ASTM standards, DCT of squeeze-cast alloy specimens was carried out by soaking them in liquid nitrogen. A vacuum flask contained the liquid nitrogen. The specimens were soaked for 4, 8 and 16 h.

3.3 XRD analysis

In order to carry out phase analysis of the alloy specimens, X-ray diffraction (RIGAKU JAPAN Model: ULTIMA-IV) was carried using CuKα (λ=1.5418A°) radiation. The scanning range for diffraction was 20-90° with a step size of 5°/min.

3.4 Optical and Scanning Electron Microscopy

The specimens for microstructural observations were prepared by standard metallographic technique. They were polished on emery papers (grades 1/0, 2/0, 3/0 and 4/0) after which cloth polishing was carried out. Etching was done using Acetic Picral (solution of 100 ml ethanol, 10ml acetic acid, 6 ml picric acid and 20 ml distilled water) and dried using ethanol. Optical micrographs were taken in OM (Model: Carl Zeiss, Germany/Axiotech, 100HD-3D) which was used to calculate volume fraction of the phases present. SEM micrographs were taken in SEM (Model: JEOL 6480 LV) equipped with energy dispersive x-ray spectroscopy (EDS) to identify the chemical composition of phases present.

3.5 Tensile test

The tensile test for all the alloys specimens (0, 4, 8 and 16 h) was performed in universal testing machine (Model: INSTRON 5967) at room temperature as per ASTM E8M-03 standard. A overhead velocity of 0.022 mm/s was maintained throughout the test. A minimum of three samples were tested and the average value was reported as tensile properties. The fracture surfaces of the broken tensile specimens were observed in FESEM (Model: FEI Nova NanoSEM 450).

3.6 Hardness test

The hardness test for all the alloy specimens was carried out on Vickers microhardness tester (Model: Leco^{TM} 248AT, USA). A load of 100gf was applied for a dwell time of 10 seconds. For each sample 7 readings were taken and hardness value was reported as average of these readings.

3.7 Wear test

The dry-sliding wear test of all the alloy specimens were performed on a Ball-on-plate wear testing machine (TR208 M1) as per ASTM G-99 standard. The machine consists of diamond type indenter. A load of 20 N was applied on the ball for a dwell time of 10 minutes. All the tests were carried out at fixed distance of 2 mm from the centre of specimen at 20 rpm. Results were obtained as wear depth (in μm) as function of sliding distance (in mm). The plate and ball were cleaned with acetone before and after the completion of test. Test was carried out twice and the average value was reported as wear depth. After the test was completed, microstructure of worn out specimen was observed under SEM.

3.8 Corrosion test

All the alloy specimens for corrosion test were grinded with silicon carbide paper (2000 and 2500 grit) and then cleaned with ethanol before carrying out corrosion test. Electrochemical corrosion tests were carried out in 0.5 wt. % NaCl solution at neutral pH and room temperature using a GillAC^{TM} potentiostat. Exposure area of 0.5 cm^2 was used throughout the tests. The corrosion cell (250 ml) consisted of three electrodes. Specimen, saturated Ag/AgCl electrode and platinum mesh were working, reference and counter electrodes respectively. Electrolyte temperature was maintained at 22±0.5°C. The potentiodynamic polarization test was carried out from -200 mV with respect to free corrosion potential at a scan rate of 0.2 mV/s. Tests lasted for 30 minutes. The Tafel curve obtained was used to calculate corrosion rate. The point of intersection from Tafel slope of cathodic branch of polarization curve and horizontal line passing through corrosion potential gave the value of current density. Corrosion rate was determined from Tafel equation.

Chapter 4

RESULTS AND DISCUSSION

4.1 Microstructural characterization

Fig. 4.1 shows the XRD patterns of untreated and all the DCT alloys. From the figure it can be observed that all the alloys consisted of peaks of 2 phases namely primary Mg (i.e. α-Mg) and Al_4RE phase. Powell et al. [5] investigated the microstructure of die-cast AE42 alloy at room temperature. They reported the presence of the same 2 phases and concluded that $Al_{11}RE_3$ and Al_4RE phases were considered same and were represented as Al_4RE phase. The XRD pattern did not consist any peak of β-$Mg_{17}Al_{12}$ phase (having MP. 437°C), which is usually present in many Mg-Al alloys. So, the β-$Mg_{17}Al_{12}$ phase is completely suppressed in the AE42 alloy, which enhances the creep properties of Mg based alloys. In this present investigation, though all the alloys consist of the same phases, the intensity some of the Al_4RE phase peaks are weak and also some of the peaks disappear in all the DCT alloys compared to the untreated alloy. These changes in the Al_4RE phase peaks indicate the reduced amount of this phase in all the DCT alloys. It was observed that the reduction in Al_4RE phase was highest in case of the DCT alloy which was soaked for 16 h. Asl et al. [6] too reported a similar variation i.e. a reduction in eutectic β-$Mg_{17}Al_{12}$ phase post DCT on AZ91 alloy. Apart from α-Mg and Al_4RE phase no other phase was detected from the XRD peaks of the DCT alloys.

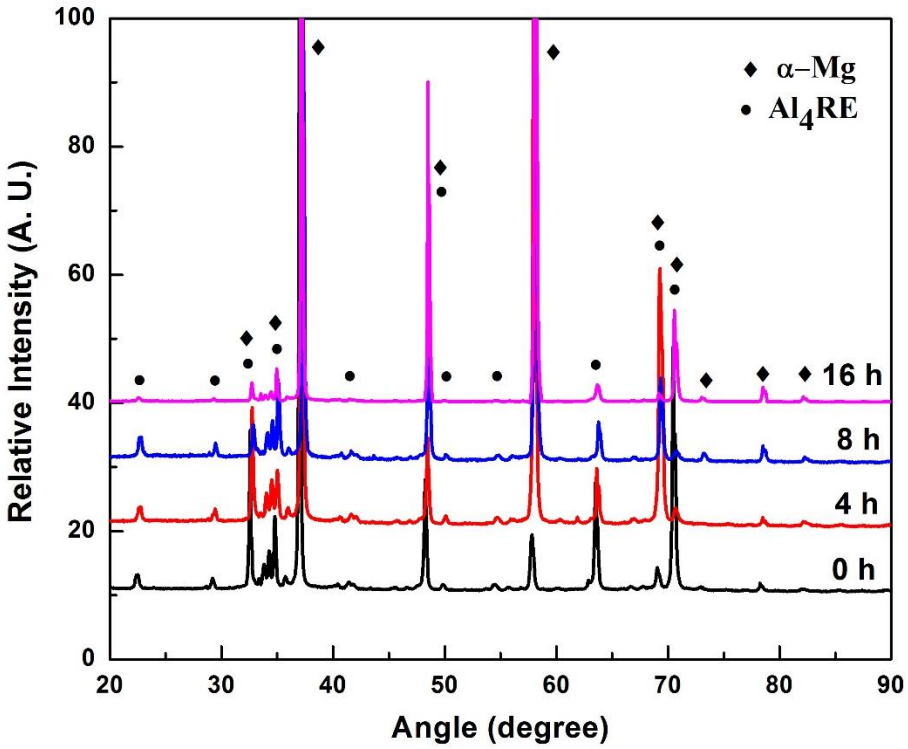

Fig. 4.1: XRD patterns obtained from all the alloys

Fig. 4.2 (a-d) exhibits the optical micrographs of all the AE42 alloys i.e. untreated and DCT alloys. It is evident from the microstructure that all the alloys consists of dendritic microstructures and the second phase which is spread at the interdendritic regions. Although the dendritic morphology remain same in all the microstructures, its volume fraction in all DCT alloys has reduced compared to the untreated alloy. A gradual decrease in the volume fraction of the Al_4RE phase can be observed from 4 h DCT to 16 h DCT alloy with 8 h DCT alloy showing the intermediate volume fraction of Al_4RE phase. The results of volume fraction analysis carried out using optical microscope shows the same as shown in Fig. 4.3, with untreated alloy showing the maximum and 16 h DCT alloy showing the least volume fraction of Al_4RE phase.

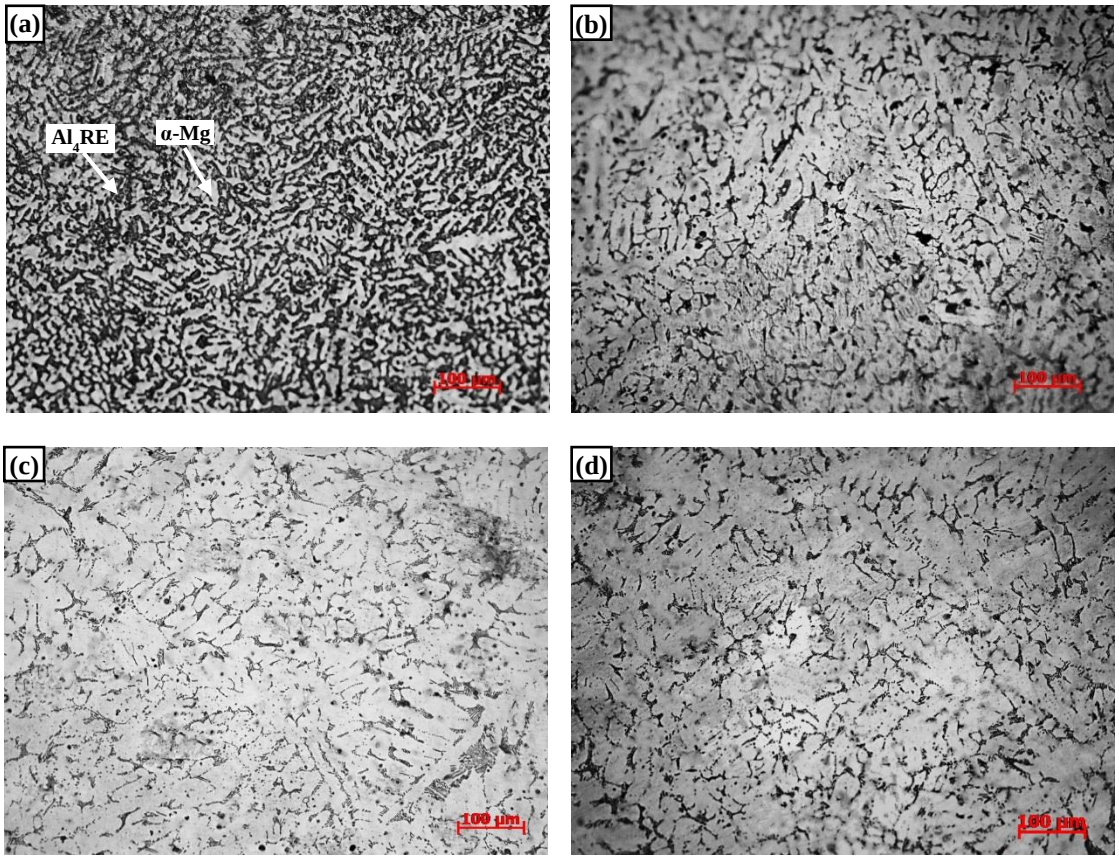

Fig. 4.2: Optical micrographs of the AE42 alloys corresponding to (a) squeeze-cast (0 h); and DCT for (b) 4 h, (c) 8 h, and (d) 16 h

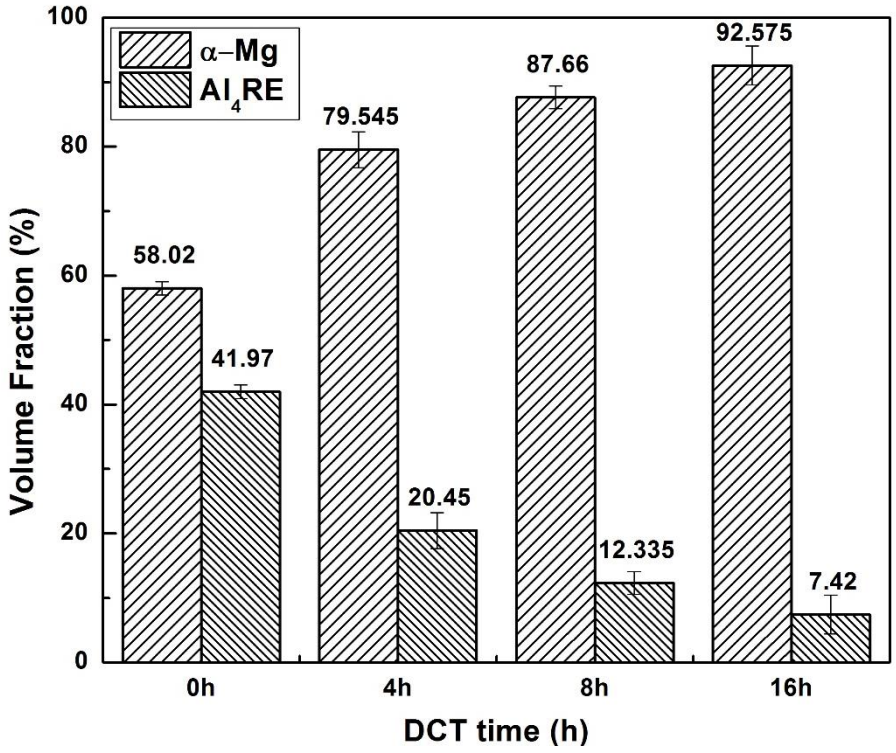

Fig. 4.3: Volume fraction (%) of the phases present in all the alloys

Fig. 4.4 (a-d) represents the SEM micrographs of the untreated and DCT AE42 alloys. The micrographs comprises of primary Mg (α-Mg) matrix surrounded by lamellar eutectic consisting of alternate layers of α-Mg and Al_4RE phases. The phases were also confirmed by EDS analysis as shown in Fig. 4.5. The untreated alloy shows nearly polygonal grains of α-Mg having a grain size of 25 µm. Mondal et al. [35] also reported the grain size of 25 µm for as-cast AE42 alloy. The phase with bright contrast is Al_4RE phase which can be observed at grain boundaries as well as at the triple points. The SEM micrograph does not show the formation of β-$Mg_{17}Al_{12}$ phase which is also confirmed by the XRD pattern. The Al_4RE phase undergoes refinement after DCT which can be observed in the micrographs. So, it can be confirmed that DCT is helping in refining the eutectic phase present on the grain boundaries. The eutectic Al_4RE phase penetrated more in the primary Mg matrix with increase in DCT time, due to which the volume fraction of α-Mg increased. Apart from penetration into the matrix the eutectic phase broke down into smaller structures. Asl et al. [6] reported a similar break down in the microstructure of AZ91 alloy following DCT.

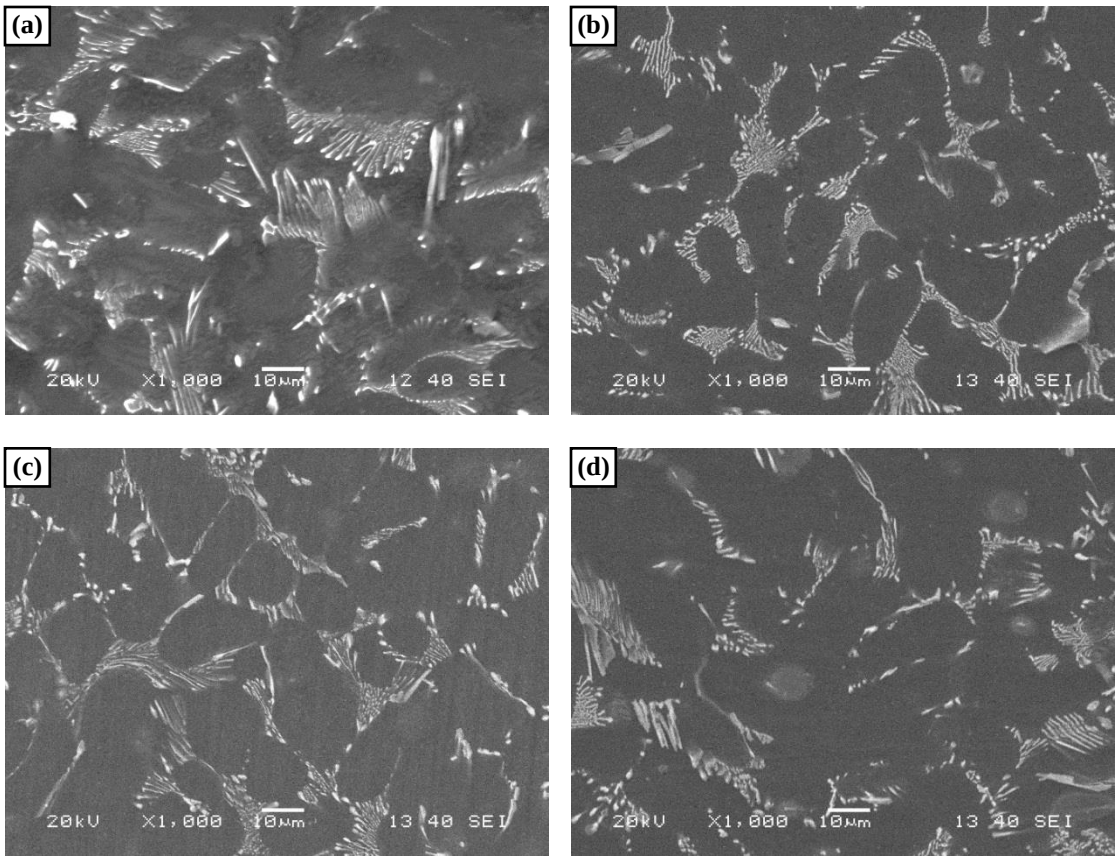

Fig. 4.4: SEM micrographs of the AE42 alloys corresponding to (a) squeeze-cast (0 h); and DCT for (b) 4 h, (c) 8 h, and (d) 16 h

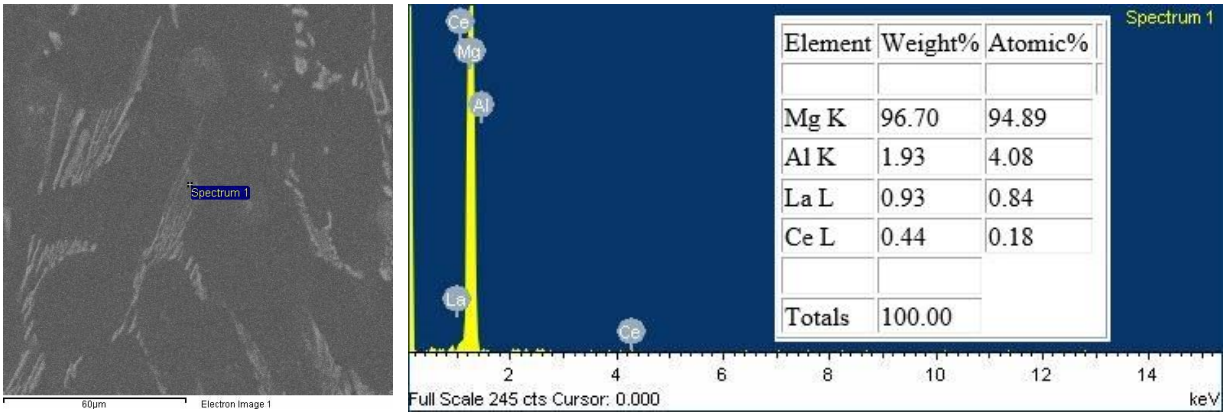

Fig. 4.5: EDS analysis carried out on the grain boundary phase present in the untreated alloy

4.2 Tensile behavior

The tensile properties of untreated and DCT alloys at room temperature are shown in Fig. 4.5 (a-b). It is evident from the figure that DCT carried out on AE42 alloy has substantial effect on its tensile properties. A drastic change can be observed on the ductility (%Elongation) and ultimate tensile strength (UTS) with a slight increase in yield strength (YS) (0.2% proof stress) of all DCT alloys compared to that for the untreated AE42 alloy. The increase in values of ductility, YS and UTS is gradual with increase in DCT time. An increase of 23.1, 51.1 and 101.8% in the values of ductility is observed for 4 h, 8 h and 16 h DCT alloys respectively. Thus, the 16 h DCT alloy showed the best tensile properties. So, it can be said that DCT has potential to significantly improve the problem of lower ductility in Mg alloys. Similar observations were made by Liu et al. [36] when they performed DCT on AZ91D alloy for 1 h, 3 h, 5 h, 6 h, 10 h and 24 h respectively. They observed that the 24 h DCT alloy showed the best ductility and UTS values among all the treated alloys. An increase of 109 % was observed in the value of ductility of 24 h treated alloy compared to the untreated alloy.

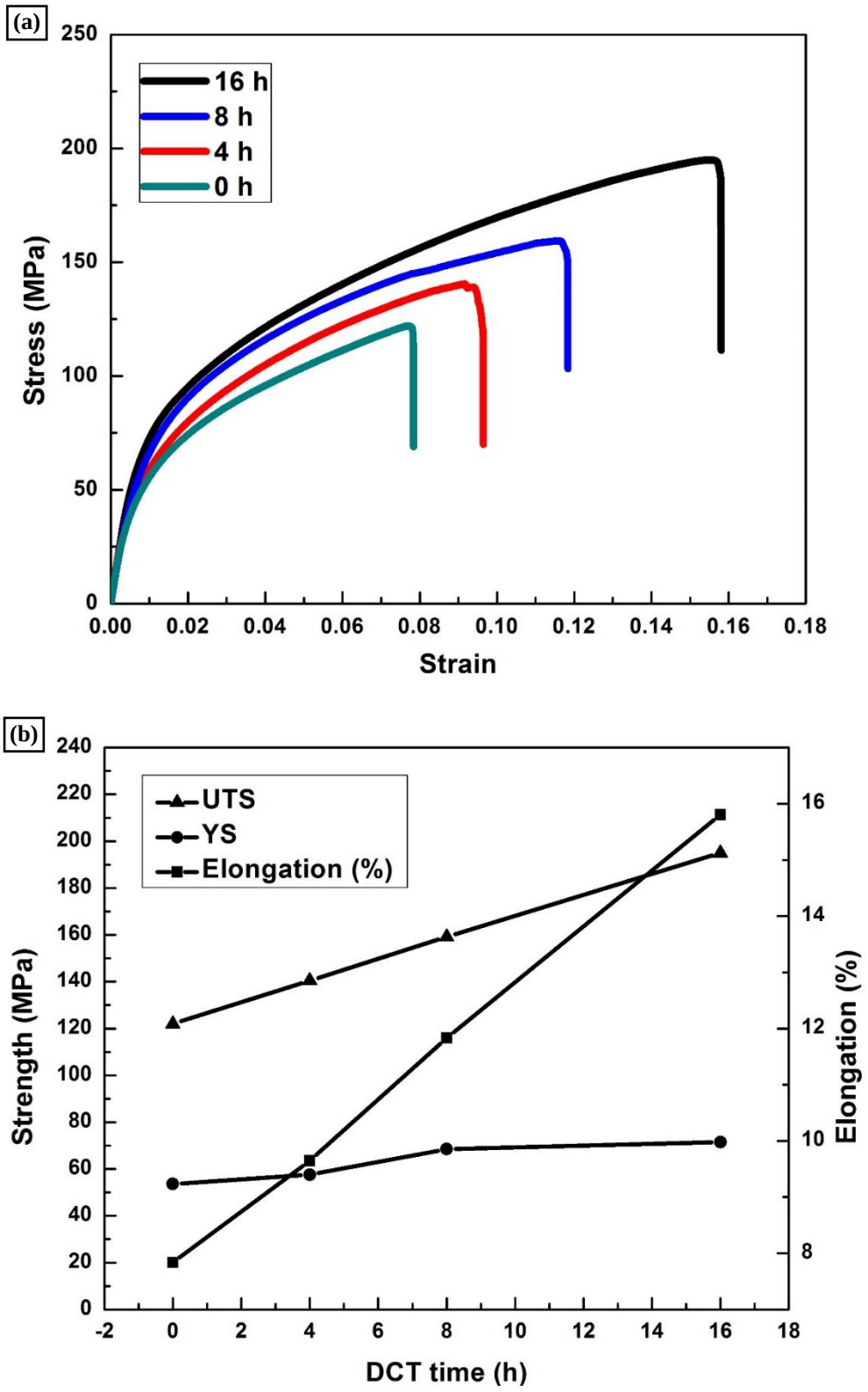

Fig. 4.6: Tensile behavior of all the alloys (a) stress-strain curve, and

(b) variation of tensile properties as a function of DCT time

The improved tensile properties of the DCT alloys can be attributed to the dissolution of Al_4RE phase present on the grain boundaries of the untreated alloy. As observed from the microstructure, amount of Al_4RE phase was the maximum in the untreated AE42 alloy. This phase is brittle in nature which is susceptible to break owing to the high brittleness. Due to its brittleness it has tendencies to cut apart the primary Mg matrix, hereby reducing the ductility and UTS of the untreated alloys. But the DCT alloys have relatively lower volume fraction of Al_4RE phase owing to which these alloys will be less brittle. The increase in solubility of Al in α-Mg with increase in DCT time from 0 to 16 h could be a probable cause for the improved tensile properties of the DCT alloys and the best tensile properties of 16 h DCT alloy can be credited to the presence of least amount of brittle Al_4RE intermetallic phase.

Fig. 4.6 (a-d) shows the micrographs of the fracture surfaces obtained from the broken tensile specimen of untreated and the DCT alloys. The fracture surface of the untreated alloy as shown in Fig. 4.6 (a) shows a distinct quasi-cleavage type of failure with many cleavage planes (shown by A) and few cleavage steps (shown by B). The presence of these in a fracture surface represents a brittle transgranular type of cleavage fracture. The river patterns (shown by C) and cleavage tongues (shown by D) are observed as plateaus and ledges on the flat facets of the cleavage planes. In general, a cleavage type of fracture begins with the formation of a number of cleavage planes. When this fracture propagates, cleavage steps are formed and network of these steps are called the river patterns, which complete the fracture. As the DCT time increases from 0 h to 16 h a larger number of quasi-cleavage planes (shown by E) can be observed in the fracture micrographs. The characteristics of ductile type fracture are micro-voids (shown by F) and plastic deformation zone (shown by G), which are present in less amount in the untreated

alloy fracture surface but an increase in their population can be observed with increase in DCT time. As an effect of DCT many shrinkage voids (shown by H) are observed in 16 h DCT alloy fracture surface. The fracture micrographs also reveal lamellar structures of Al_4RE (shown by I) which were confirmed by EDS analysis. It is also evident that their presence in the fracture micrographs is reduced with the increase in DCT time.

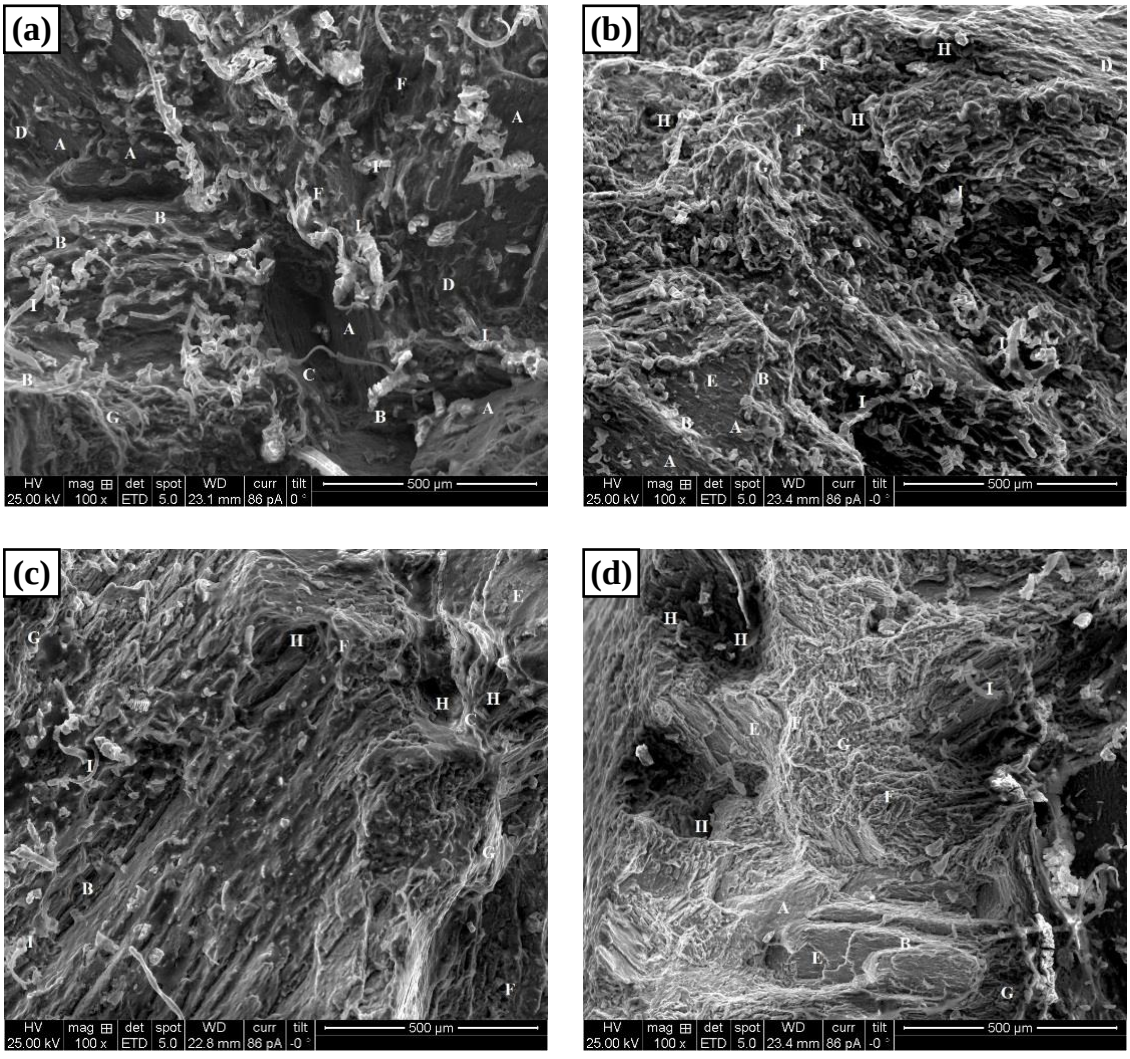

Fig 4.7: SEM micrographs of the fracture surfaces of the broken tensile specimens of the AE42 alloy corresponding to (a) squeeze-cast (0 h); and DCT for (b) 4 h, (c) 8 h, and (d) 16 h

4.3 Hardness

The deviation in the average microhardness values for all the alloys is shown in Fig. 4.7. It is evident from the figure that among all the alloys used in the present investigation, untreated alloy shows highest hardness value. Compared to the untreated alloy, the DCT alloy exhibited lower hardness values. The hardness values of DCT alloys decreased with increase in DCT time from 4 to 16 h. Thus, it can be said that DCT has a significant influence on the hardness of the AE42 alloy. The Al_4RE phase is hard compared to the α-Mg phase and as the untreated alloy has highest amount of Al_4RE phase among all the alloys, it shows superior hardness. So, the lower hardness values of DCT alloy can be attributed to the presence of lower volume fraction of Al_4RE phase.

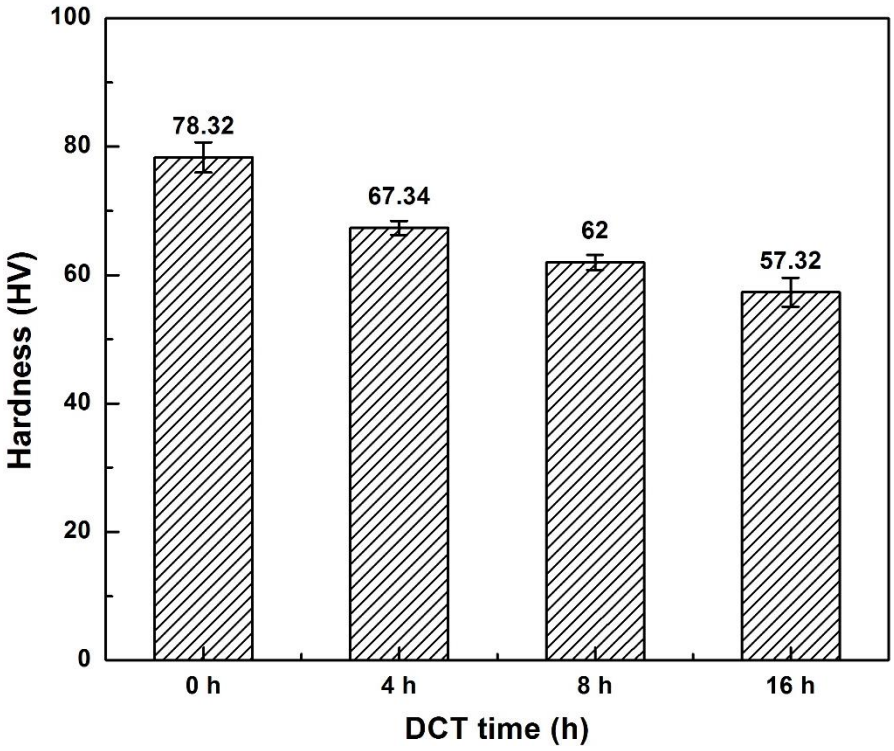

Fig. 4.8: Variation of microhardness of all the alloys

4.4 Wear behavior

Fig. 4.8 shows the wear behavior of the untreated and DCT alloys, plotted as wear depth (in µm) vs. sliding distance (in mm). It is evident from the curve that untreated alloy exhibits lowest wear depth compared to all the DCT alloys. Among all the DCT alloys, 4 and 16 h DCT alloy exhibits the lowest and highest wear depths respectively with 8 h DCT alloy having intermediate wear depth. Wear depth shows an inverse proportionality with wear resistance. So, the 16 h DCT and untreated alloy exhibited the lowest and highest wear resistance respectively.

The SEM micrographs of the worn surfaces of untreated and DCT alloys are shown in Fig. 4.9. The micrographs reveal many continuous parallel grooves on the worn surfaces. The track width as calculated from the SEM micrographs of the worn surfaces are shown in Fig. 4.10. The track width increased from 0 to 16 h DCT alloy. The grooves present on the worn surface of 16 h DCT alloy were not only deeper and wider but also more in number. The presence of these parallel grooves can be attributed to the microploughing phenomena. Also, the continuity in the grooves in the direction of sliding of indenter is a proof of abrasion mechanism of wear. Moreover, the worn surface of 16 h DCT alloy more asymmetrical debris scattered out from the wear track, compared to the untreated alloy. It is obvious that owing to the lower hardness of the DCT alloys compared to the untreated alloys, lower wear resistance of DCT alloys is obtained.

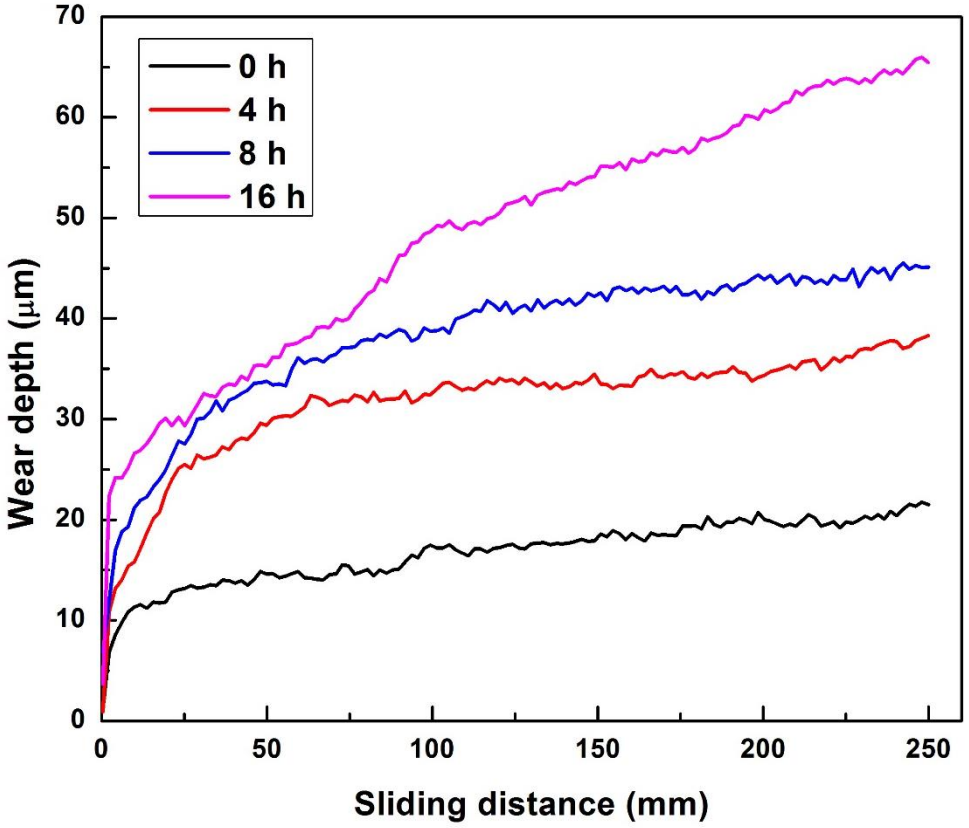

Fig. 4.9: Variation of wear depth of all the AE42 alloys with sliding distance

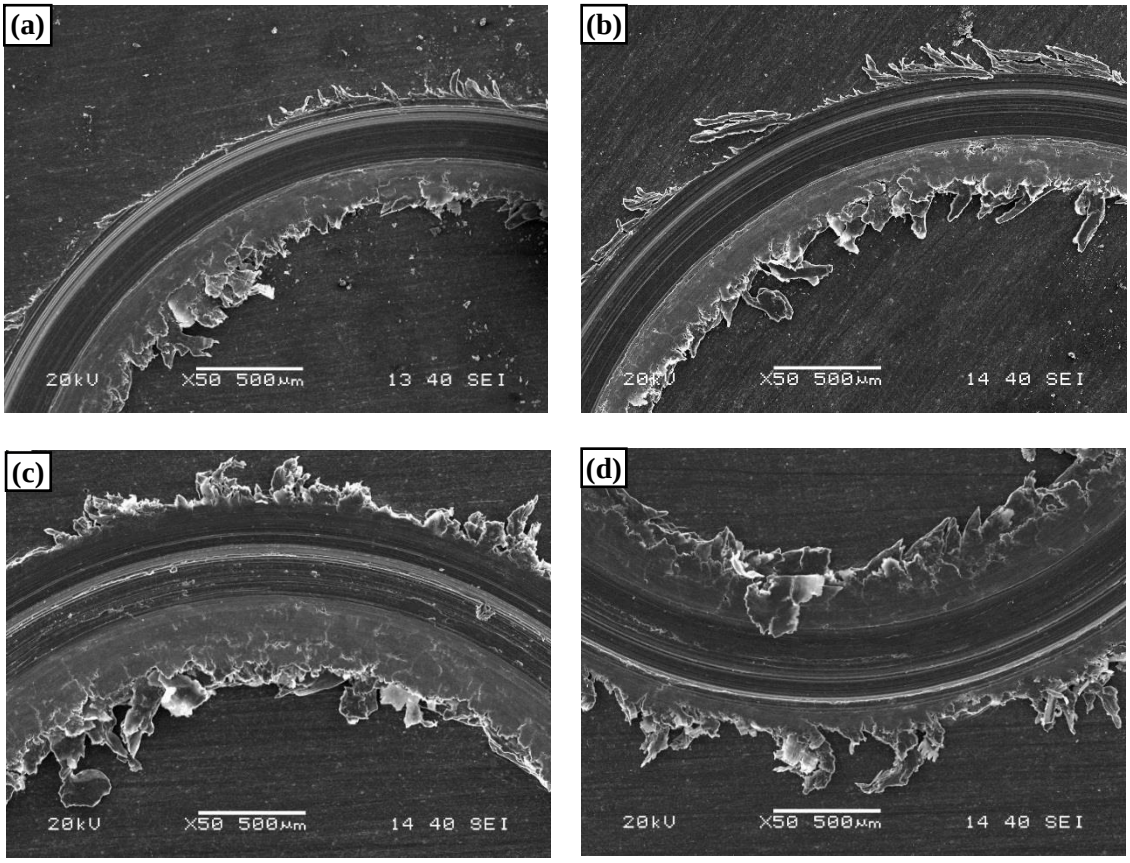

Fig. 4.10: SEM micrographs of the worn surfaces corresponding to (a) squeeze-cast (0 h); and DCT for (b) 4 h, (c) 8 h, and (d) 16 h

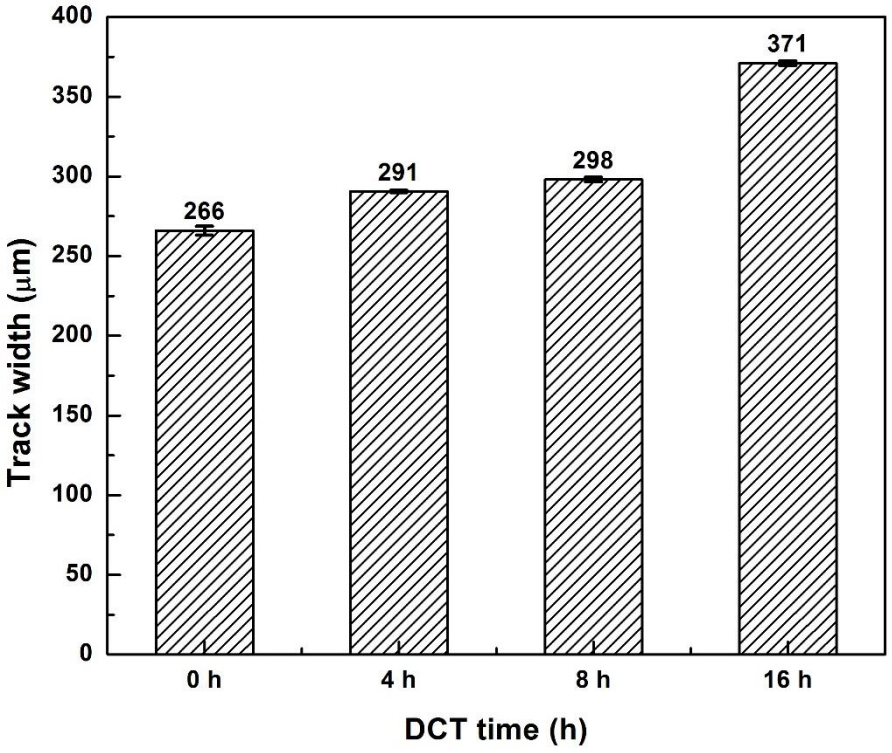

Fig. 4.11: Variation of wear track width with DCT time of all the alloys

4.5 Corrosion behavior

The results of potentiodynamic polarization test performed on all the alloys are shown in Fig. 4.11 and the corrosion rates calculated from it are shown in Fig. 4.12. It is evident from the figure that the untreated alloys showed lowest corrosion rate (nearly 0.68 mm/yr). All the DCT alloys had higher corrosion rates compared to the untreated alloy with 16 h DCT alloy showing the highest corrosion rate (nearly 0.95 mm/yr). The chloride ions (Cl^-) formed during electrochemical reaction has a tendency to break down the protective film formed over the surface of alloy. Owing to the formation of relatively passive film over the untreated alloy, the DCT alloys exhibited lower corrosion rates. The XRD patterns of the corroded surfaces of the all the alloys are shown in Fig. 4.13. The plot confirms $Mg(OH)_2$ as corrosion product. The DCT alloys showed prominent peaks of $Mg(OH)_2$ compared to the untreated alloy with 16 h DCT alloy exhibiting highest intensity of $Mg(OH)_2$ peaks thus signifying more corrosion in the DCT alloys. The α-Mg phase is more anodic in nature compared to Al_4RE phase owing to which it gets removed from the specimen surfaces following corrosion. Fig. 4.14 represents the SEM micrographs of the corroded surfaces of all the alloys. The corroded surface of untreated alloy revealed the presence of thin and uniform corroded film. However, the corroded film present on the DCT alloys was relatively discontinuous and uneven due to which corrosion resistance of all DCT alloys reduced.

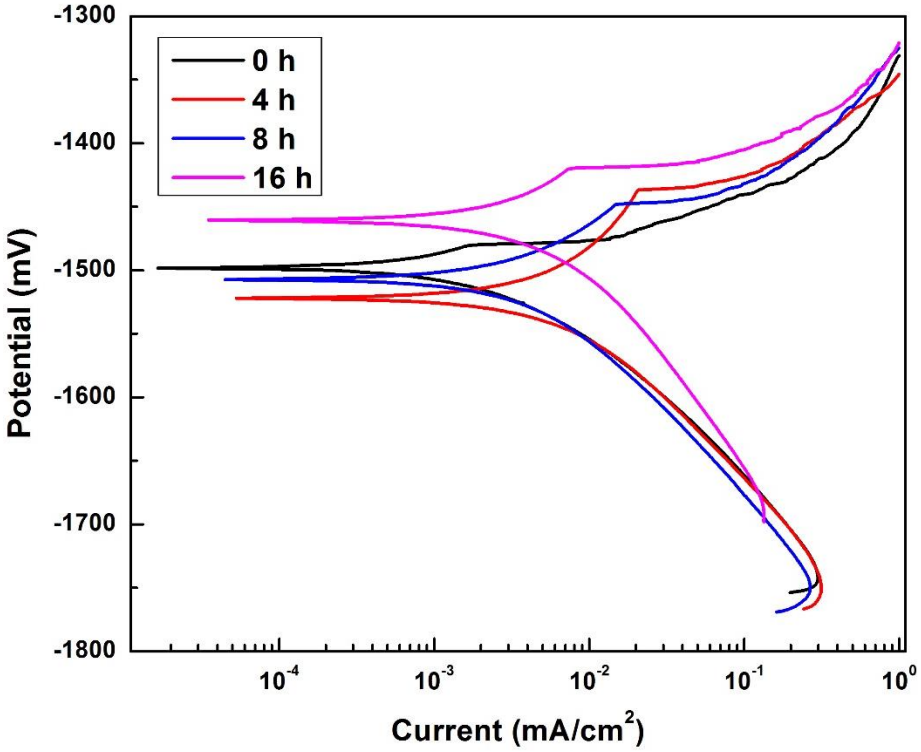

Fig. 4.12: Results of potentiodynamic polarization test on all the alloys

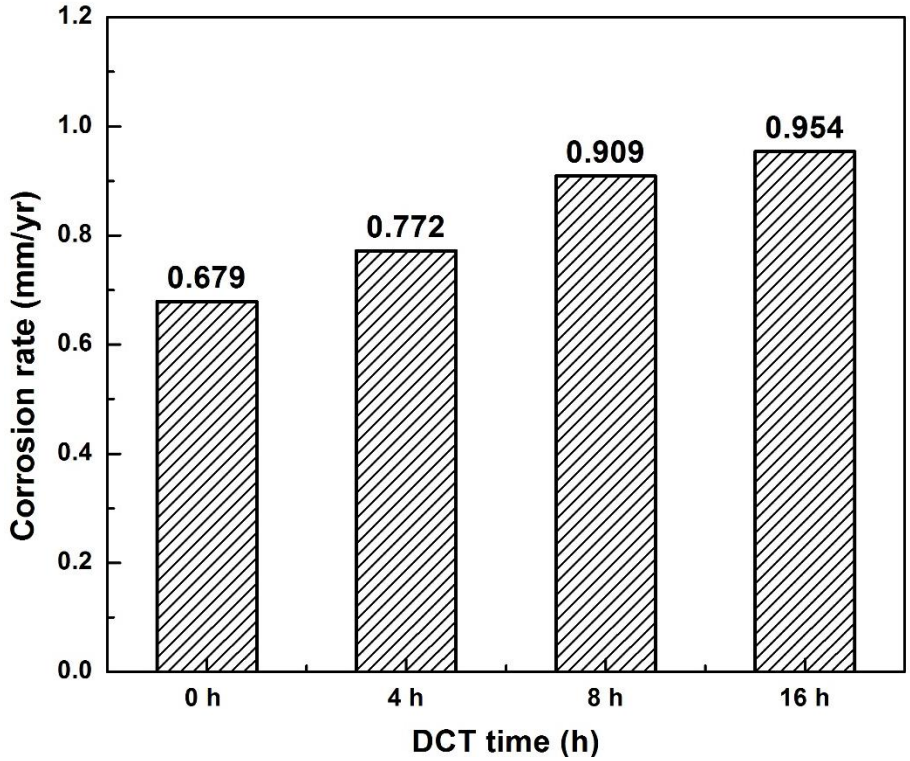

Fig. 4.13: Variation of corrosion rate calculated from the potentiodynamic polarization plots for all the alloys

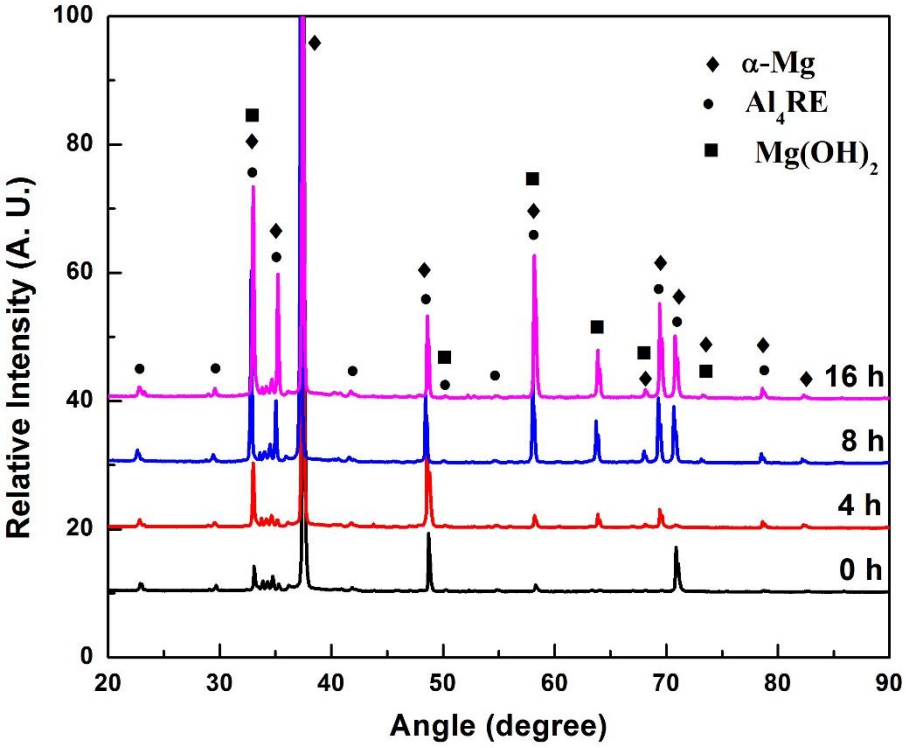

Fig. 4.14: XRD patterns obtained from corroded surfaces all the alloys

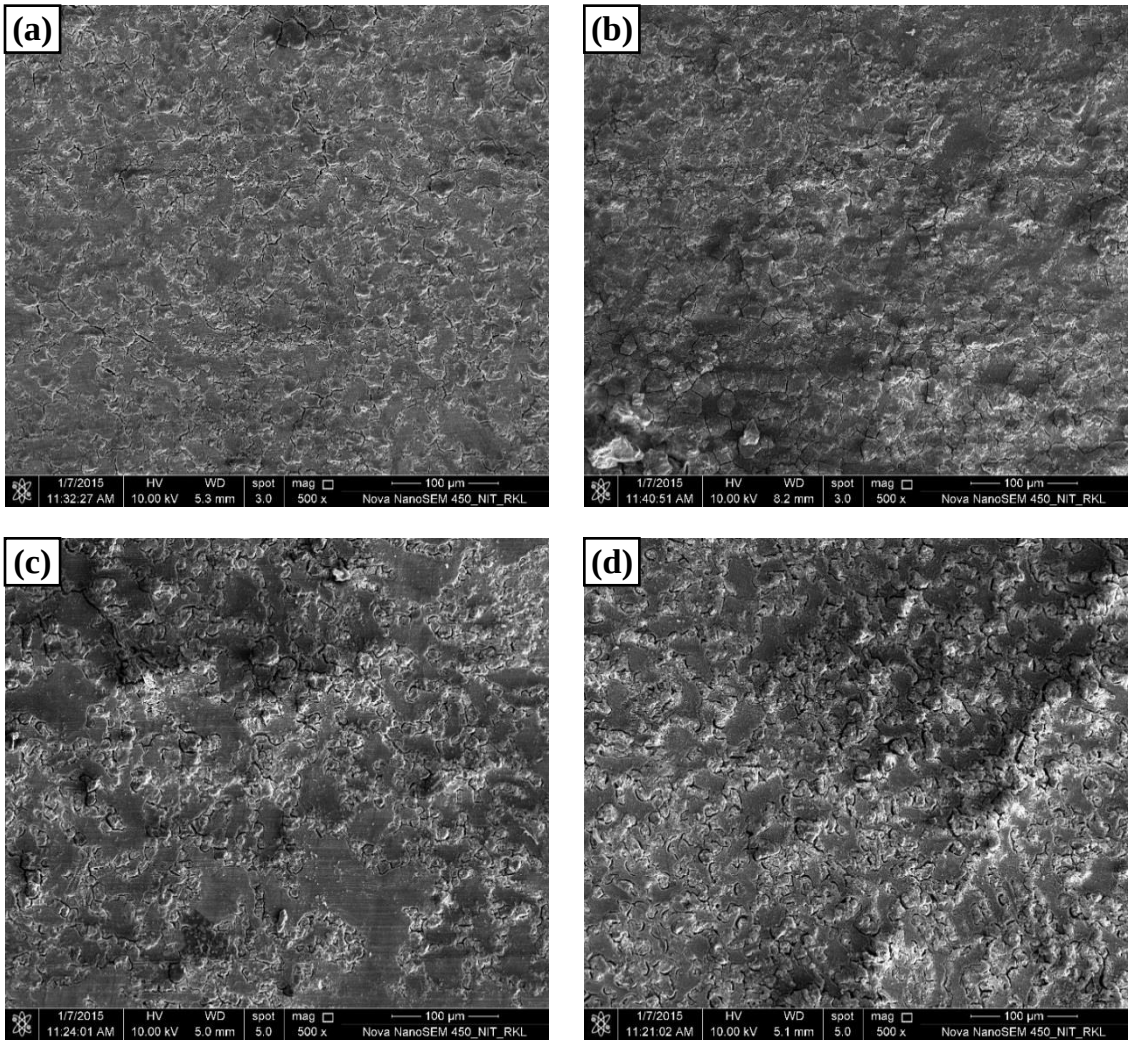

Fig. 4.15: SEM micrographs of the corroded surfaces of the AE42 alloy corresponding to (a) squeeze-cast (0 h); and DCT for (b) 4 h, (c) 8 h, and (d) 16 h

Neubert et al. carried out potentiodynamic polarization test on Mg-RE based alloy, to investigate the corrosion resistance of different alloys (with change in RE wt.%) [37]. They concluded that increased RE addition was responsible for reduced corrosion resistance. The intermetallic Al_4RE phase present on the grain boundaries being more resistant to corrosion than the α-Mg phase tends to increase the overall corrosion resistance of the alloy [38]. Similarly, in this investigation due to reduced volume% of corrosion resistant Al_4RE phase on the grain boundaries of the DCT alloys, which could be the plausible cause of poor corrosion resistance following DCT.

Chapter 5

CONCLUSIONS

5.1 Conclusions

In the present investigation the effect of DCT on the microstructure and mechanical properties including corrosion behavior of the creep resistant squeeze-cast AE42 alloy were examined. For comparison, the same was also studied on the AE42 alloy without DCT. The following conclusions are drawn:

i. Both the untreated and DCT alloys consisted primary Mg (α-Mg) and lamellar eutectic consisting of alternate layers of α-Mg and Al_4RE phases.

ii. The volume fraction of the Al_4RE phase present in the AE42 alloy reduced gradually with increase in DCT time from DCT from 4 to 16 h.

iii. The ductility and UTS of all the DCT alloys increased significantly with a marginal increase in YS. The improvement in ductility was attributed to the dissolution of the brittle Al_4RE phase following DCT. The increased YS was attributed to the solid solution strengthening. Among the alloys employed the best tensile properties were obtained for the 16 h DCT alloy owing to its lowest content of the brittle Al_4RE phase.

iv. The hardness and wear resistance of the alloys subjected to DCT reduced due to presence of reduced volume fraction of the harder Al_4RE phase.

v. The untreated alloy exhibited the best corrosion resistance among the alloys employed. The DCT alloys revealed relatively poor corrosion resistance, which was attributed to the reduced amount of the Al_4RE phase.

References

[1] A.A. Nayeb-Hashemi, J.B. Clark, Phase Diagrams of Binary Magnesium Alloys, ASM International, Metal Park (1998) 43.

[2] I.P. Moreno, T.K. Nandy, J.W. Jones, J.E. Allison, T.M. Pollock, Scr. Mater. 48 (2003) 1029.

[3] A.A. Luo, Int. Mater. Rev. 49 (2004) 13.

[4] M.O. Pekguleryuz, A.A. Kaya, Adv. Eng. Mater. 5 (2003) 866.

[5] B.R. Powell, V. Rezhets, M.P. Balogh, R. A. Waldo, J. Mater. 54 (2002) 34.

[6] K.M. Asl, A. Tari, F. Khomamizadeh, Mater. Sci. Eng. A 523 (2009) 27.

[7] P. Baldissera, C. Delprete, Open Mech. Eng. J. 2 (2008) 1.

[8] V. Wesling, Mater. Sci. Eng. A 462 (2007) 144.

[9] Y. Wu, W. Hu, Res. Lett. Phys. (2008) 1.

[10] H.E. Friedrich, B.L. Mordike, Magnesium Technology-Metallurgy, Design Data, Applications, Springer (2006) 18.

[11] J. Abthoff, W. Gelsw, J. Lang, in:, Proc. Third Int. Magnes. Conf., Manchester, UK (1996).

[12] E. Aghion, B. Bronfin, D. Eliezer, S. Schumann, in:, Proc. Second Osaka Int. Conf. Platf. Sci. Technol., Osaka, Japan (2003).

[13] F. Zimmermann, Volkswagen AG (2002) 56.

[14] J. Mizrahi, Airpower 25(3) (1998) 1.

[15] V.A. McLean, in:, Proc. Int. Magnes. Conf. (1995).

[16] M.P. Staiger, A.M. Pietak, J. Huadmai, G. Dias, Biomater. 27 (2006) 1728.

[17] Y.W. Song, D.Y. Shan, R.S. Chen, F. Zhang, E.H. Han, Mater. Sci. Eng. C 29 (2009) 1039.

[18] Y.W. Song, D.Y. Shan, E.H. Han, Mater. Lett. 62 (2008) 3276.

[19] J.S. Waltrip, in:, Proc. 47th Ann. World Magnes. Conf., Cannes (1990) 124.

[20] W.E. Mercer, SAE Tech. (1990) 900788.

[21] N.R. Neelameggham, H.I. Kaplan, B.R. Powell, TMS Magnesium Technology, Warrendale, PA (2005) 53.

[22] Y. Lü, Q. Wang, X. Zeng, W. Ding, C. Zhai, Y. Zhu, Mater. Sci. Eng. A 278 (2000) 66.

[23] J. Zhang, D. Zhang, Z. Tian, J. Wang, K. Liu, H. Lu, D. Tang, J. Meng, Mater. Sci. Eng. A 489 (2008) 113.

[24] M.M. Avedesian, H. Baker, ASM Specialty Handbook- Magnesium and Magnesium Alloys, ASM International, Materials Park (1999) 24.

[25] H. Friedrich, S. Schumann, J. Mater. Process. Technol. 117 (2001) 276.

[26] J. Tao, Y. Zhang, F. Fan, Q. Chen, Def. Technol. 9 (2013) 146.

[27] S. Zhirafar, a. Rezaeian, M. Pugh, J. Mater. Process. Technol. 186 (2007) 298.

[28] V. Leskovšek, M. Kalin, J. Vižintin, Vacuum 80 (2006) 507.

[29] F.J. da Silva, S.D. Franco, E.O. Ezugwu, M. Souza Jr., Wear 261 (2006) 674.

[30] J.Y. Huang, Y.T. Zhu, X.Z. Liao, I.J. Beyerlein, M.A. Bourke, T.E. Mitchell, Mater. Sci. Eng. A 339 (2003) 241.

[31] J. Indumathi, J. Bijwe, A.K. Ghosh, M. Fahim, N. Krshnaraj, Wear 225-229 (1999) 343.

[32] K.E. Lulay, K. Khan, D. Chaaya, J. Mater. Eng. Perform. 11 (2002) 479.

[33] J.A. Bailey, J. Barsom, P. Blau, ASM Handbook: Mechanical Testing and Evaluation (2007) 38.

[34] H. Ackerman, D.R. Adolphson, D.C. Agarwal, ASM Handbook: Corrosion (1992) 154.

[35] A.K.Mondal, C. Blawert, S. Kumar, Mater. Corros. (2015) doi: 10.1002/maco.201408071.

[36] J. Liu, G. Li, D. Chen, Z. Chen, Chinese J. Aeronaut. 25 (2012) 931.

[37] V. Neubert, I. Stulakova, B. Smola, A. Bakkar, B.L. Mordike, Kov. Mater. 42 (2004) 31.

[38] C. Blawert, E. Morales, H. Dieringa, N. Hort, M.A. Azeem, S. Kumar, in:, Fourteenth Symp. Verbundwerkstoffe Und Werkstoffverbunde, Viena, Austria (2003) 159.